



Different Photoisomerization Routes Found in the Structural Isomers of Hydroxy Methylcinnamate

Journal:	<i>Physical Chemistry Chemical Physics</i>
Manuscript ID	CP-ART-01-2018-000414.R2
Article Type:	Paper
Date Submitted by the Author:	02-Apr-2018
Complete List of Authors:	Kinoshita, Sin-nosuke; Hiroshima University, Department of Chemistry Miyazaki, Yasunori ; Hiroshima University, Department of Chemistry Sumida, Masataka; Hiroshima University, Department of Chemistry Onitsuka, Yuuki; Hiroshima University, Department of Chemistry Kohguchi, Hiroshi; Hiroshima Daigaku, Inokuchi, Yoshiya; Hiroshima University, Department of Chemistry Akai, Nobuyuki; Tokyo University of Agriculture and Technology, Shiraogawa, Takafumi; Sokendai Ehara, Masahiro; Institute for Molecular Science, Yamazaki, Kaoru; Institute for Materials Research, Tohoku University Harabuchi, Yu; Hokkaido University, Department of Chemistry, Faculty of Science; JST, PRESTO, Maeda, Satoshi; Faculty of Science, Hokkaido University, Chemistry Taketsugu, Tetsuya; Hokkaido Univ, Department of Chemistry, Faculty of Science Ebata, Takayuki; Hiroshima University, Chemistry

Different Photoisomerization Routes Found in the Structural Isomers of Hydroxy Methylcinnamate

Sin-nosuke Kinoshita,¹ Yasunori Miyazaki,¹ Masataka Sumida,¹ Yuuki Onitsuka,¹ Hiroshi Kohguchi,¹ Yoshiya Inokuchi,¹ Nobuyuki Akai,² Takafumi Shiraogawa,³ Masahiro Ehara,^{3,4*} Kaoru Yamazaki,^{5*} Yu Harabuchi,⁶ Satoshi Maeda,⁶ Tetsuya Taketsugu,⁶ and Takayuki Ebata^{1*}

¹*Department of Chemistry, Graduate School of Science, Hiroshima University, Higashi-Hiroshima 739-8526, Japan*

²*Graduate School of Bio-Applications and Systems Engineering (BASE), Tokyo University of Agriculture and Technology, Naka-cho, Koganei, Tokyo 184-8588, Japan*

³*SOKENDAI, the Graduate University for Advanced Studies, Hayama-cho, Kanagawa 240-0193, Japan*

⁴*Institute for Molecular Science and Research Center for Computational Science, 38 Myodaiji, Okazaki 444-8585, Japan*

⁵*Institute for Materials Research, Tohoku University, Katahira 2-1-1, Aoba-ku, Sendai, 980-8577, Japan*

⁶*Department of Chemistry, Faculty of Science, Hokkaido University, Sapporo 060-0810, Japan*

*(K. Y.) kaoru.yamazaki@imr.tohoku.ac.jp

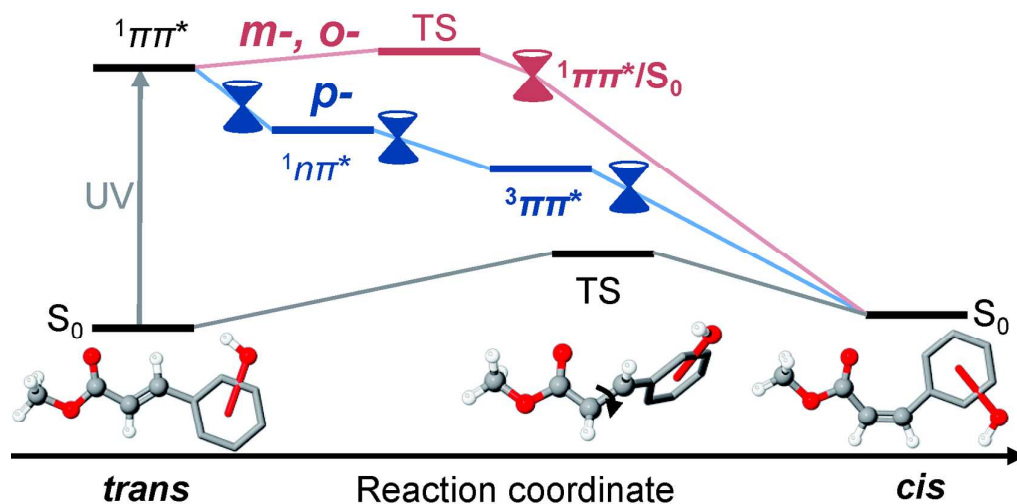
*(M. E.) ehara@ims.ac.jp

*(T. E.) tebata@hirohsima-u.ac.jp

Abstract: An experimental and theoretical study has been carried out to elucidate the nonradiative decay (NRD) and *trans* (E) \rightarrow *cis* (Z) isomerization from the S_1 ($^1\pi\pi^*$) state of structural isomers of hydroxy methylcinnamate (HMC); *ortho*-, *meta*- and *para*-HMC (*o*-, *m*- and *p*-HMC). A low temperature matrix-isolation Fourier Transform Infrared (FTIR) spectroscopic study revealed that all the HMCs are *cis*-isomerized upon uv irradiation. Variety of laser spectroscopic methods have been utilized for jet-cooled gas phase molecules to investigate the vibronic structure and lifetimes of the S_1 state, and to detect the transient state appearing in the NRD process. In *p*-HMC, the zero-point level of the S_1 state decays as short as 9 ps. A transient electronic state reported by Tan *et al.* (*Faraday Discuss.* **2013**, *163*, 321–340) was reinvestigated by nanosecond UV-tunable deep UV pump-probe spectroscopy and was assigned to the T_1 state. For *m*- and *o*-HMC, the lifetime at zero-point level of S_1 is 10 ns and 6 ns, respectively, but becomes substantially shorter at an excess energy higher than 1000 cm^{-1} and 600 cm^{-1} , respectively, indicating the onset of NRD. Different from *p*-HMC, no transient state (T_1) was observed in *m*- nor *o*-HMC. These experimental results are interpreted with the aid of TDDFT calculations by considering the excited-state reaction pathways and the radiative/nonradiative rate constants. It is concluded that in *p*-HMC, the *trans* \rightarrow *cis* isomerization proceeds via a [*trans*- $S_1 \rightarrow ^1n\pi^* \rightarrow T_1 \rightarrow cis$ - S_0] scheme. On the other hand, in *o*- and *m*-HMC, the isomerization proceeds via a [*trans*- $S_1 \rightarrow$ twisting along the C=C double bond to 90° on $S_1 \rightarrow cis$ - S_0] scheme. The calculated barrier height along the

twisting coordinate agrees well with the observed onset of the NRD channel for both *o*- and *m*-HMC.

TOC figure and sentence: Upon the uv excitation, *meta*- and *ortho*-hydroxy methylcinnamate (*m*-, *o*-HMC) isomerize via [*trans*- $^1\pi\pi^*$ \rightarrow TS \rightarrow *cis*- S_0] route, while *para*-HMC(*p*-HMC) isomerizes via [*trans*- $^1\pi\pi^*$ \rightarrow $^1n\pi^*$ \rightarrow $T_1(^3\pi\pi^*)$ \rightarrow *cis*- S_0] route.



1. Introduction

The electronic structure and nonradiative decay (NRD) of the excited states of coumaric acid and its derivatives have attracted attention for their unique photoreactivity.¹⁻⁴ Some of the experimental and theoretical studies address the issue of Photoactive Yellow Protein (PYP) found in *Halorhodospina halophila*, where the *trans* (E) \rightarrow *cis* (Z) photoisomerization of *p*-coumaric acid triggers its negative phototaxis behavior against blue light.⁵⁻⁸ The chromophore was studied in order to elucidate the role of the hydrogen-bond network⁹⁻¹² and of proton transfer,^{13,14} as well as of the partially anionic form, under the

protein environment.^{15–19} However, different excited state dynamics of the chromophore is expected between the gas phase and the protein environment due to the inscrutable $^1n\pi^*$ state.^{20–22}

Gas-phase spectroscopic study on methylcinnamate was first performed by Ebata *et al.* to elucidate the Diels-Alder reaction mechanism.^{23,24} They observed a strong correlation between the S_1 lifetime and the excess photon energy, suggesting that the correlation is related to the barrier of NRD to the $^1n\pi^*$ state. On the other hand, Lewis *et al.* studied the influence of a molecular structure that blocks the double bond twist (or Rotation Blocked – Methylcinnamate) on the excited state dynamics by picosecond fluorescence spectroscopy.²⁵ They reported that the photoisomerization could occur in the singlet excited state *via* direct isomerization or internal conversion (IC). Similar results were obtained by femtosecond transient absorption spectroscopy.²⁶

Instead of the prototype cinnamate, substituted cinnamates have been extensively studied experimentally and theoretically. The hydroxy methylcinnamate (HMC) and methoxy methylcinnamate (MMC) series have been studied computationally by Ehara and coworkers, who suggest that the energy barrier for NRD may come from the double bond twist in the S_1 state and that the barrier height depends on the substituted position.^{27,28} In addition, another NRD pathway *via* IC to the $^1\pi\sigma^*$ state has also been theoretically suggested for caffeic acid, which has a catechol-like ring structure, by Karsili *et al.*²⁹ Experimentally, Buma and

coworkers measured the S_1 - S_0 electronic spectra of *p*-HMC and *p*-MMC in the gas phase under jet-cooled conditions.^{30,31} They found a transient electronic state with lifetime of 29.3 and 27 ns for *p*-HMC and *p*-MMC, respectively, by using nanosecond pump-probe spectroscopy with a 193 nm ArF laser for the probe ionization. They suggested that the observed transient state may be the $^1n\pi^*$ state generated by IC from S_1 . However, Ebata and coworkers reported a conflicting result by measuring the S_1 lifetime of *p*-MMC and its 1:1 complex with H_2O . They found that hydrogen-bonding to the carbonyl oxygen shortens the S_1 lifetime compared to the monomer, although the calculated potential energy curves predicted a larger barrier height for the S_1 - $^1n\pi^*$ potential curve crossing in the complex.³² In addition, They reported that hydration of the OH group of *p*-HMC increases the S_1 lifetime by three orders of magnitude.³³ As a result of these findings, Cui and coworkers recently reported a MS-CASPT2//SA-CASSCF study on *p*-HMC, *p*-MMC and their 1:1 complex with water.^{34,35} They suggested that two competing NRD pathways for S_1 exist: IC to $^1n\pi^*$ and direct isomerization on the S_1 surface. The former is dominant for the monomer and the latter for the complex. The IC decay route from S_1 ($\pi\pi^*$) to $^1n\pi^*$ in cinnamate derivatives has been widely supported by several groups.³⁶⁻³⁸ Very recently, Ebata and coworkers carried out an experiment similar to that of Buma *et al.* for *p*-MMC with a tunable deep UV (DUV) laser for the ionization scheme to assign the transient state.³⁹ With an aid of theoretical calculations, they concluded that the observed transient state is the T_1 state generated by the successive [S_1

$\rightarrow {}^1n\pi^* \rightarrow T_2 \rightarrow T_1$] decay process, where the whole process to generate T_1 is completed within 1 ns. Furthermore, Ebata *et al.* confirmed the formation of the *cis*-cinnamate as a final product upon the UV irradiation of *p*-MMC by low-temperature matrix-isolation FTIR spectroscopy.⁴⁰ However, it is not still clear whether the latter route, direct isomerization on the S_1 surface, exists in some cinnamate derivatives.

In this paper, we report our study of the photochemistry of the structural isomers of HMC, *o*-, *m*- and *p*-HMC, under cold isolated conditions in Ne matrix and in the gas phase to elucidate the substitution effect on the mechanism of isomerization. Low-temperature matrix-isolation FTIR spectroscopy was utilized to investigate the photoproduct after UV excitation. A comparison of the observed IR spectra of the products with calculated spectra from density functional theory (DFT) revealed that all the species isomerize upon the uv irradiation. On the other hand, the lifetime of the S_1 state shows remarkable difference between *p*-HMC and *m*-, *o*-HMC; the S_1 lifetimes of *m*-, *o*-HMC are ~ 1000 times longer than *p*-HMC at zero-point vibrational level and show clear onset of lifetime shortening at an excess energy of 1000 cm^{-1} in *m*-HMC and 600 cm^{-1} in *o*-HMC. A nanosecond UV- tunable DUV pump-probe spectroscopic measurement revealed the appearance of the transient T_1 state in *p*-HMC but not in *m*-, or *o*-HMC. The experimentally observed NRD and isomerization processes are analyzed by systematic NRD pathway search calculations combined with time-dependent density functional theory (TDDFT) by use of the global

reaction route mapping (GRRM) method^{41,42}. Based on these studies, we discuss the possible mechanisms of NRD leading to *trans* → *cis* photoisomerization for *o*-, *m*- and *p*-HMC.

2. Experimental

2.1 Laser spectroscopy and S₁ lifetime measurement in the gas phase

The experimental setup used for the laser spectroscopy has been described previously.^{32,33,39} Briefly, solid HMC in a sample housing attached to the head of a pulsed nozzle was heated for vaporization and diluted with He carrier gas at a total pressure of 1.5 bar. The gaseous mixture was expanded into vacuum through the 1 mm orifice of a pulsed nozzle to produce a supersonic free jet. The S₁-S₀ electronic spectra were recorded by laser induced fluorescence (LIF) and mass-resolved resonance two photon ionization (R2PI) spectroscopic methods.

In the LIF measurement, tunable UV laser light was generated by second harmonics generation (SHG) of the output of a Nd³⁺:YAG laser-pumped dye laser (Lambda Physik Scanmate/Continuum Surelite II) and was introduced into the vacuum chamber to cross the supersonic free jet ~20 mm downstream of the orifice. The LIF spectra were obtained by detecting the total fluorescence with a photomultiplier tube as a function of the UV frequency. UV-UV hole-burning (UV-UV HB) spectroscopy by using hole-burn (HB) and probe lasers was carried out to discriminate the bands of coexisting isomers. The UV-UV HB spectra are obtained as depletions in the fluorescence intensity due to ground state depopulation induced

by the HB laser. Mass-resolved R2PI measurements were performed in a molecular beam vacuum chamber. The supersonic free jet was skimmed by a skimmer located 50 mm downstream of the nozzle and the molecules in the beam were ionized by R2PI *via* the S_1 state. For *o*-HMC and *m*-HMC, a two-color (2C) R2PI scheme was necessary because in both cases the S_1 electronic state is located at less than half of the first ionization potential (IP_0). The ions were mass-selected using a time-of-flight (TOF) spectrometer and detected with a channeltron. The R2PI spectra were obtained by plotting the mass-selected ion signal as a function of the UV frequency. The lifetimes of the vibronic levels in the S_1 state were obtained by either the nanosecond or the picosecond pump-probe spectroscopic measurement.

The experimental setup for the picosecond time-resolved pump-probe spectroscopy has been described in our previous papers.^{32,33} Briefly, two tunable picosecond UV pulses with different wavelengths were obtained by second harmonic generation (SHG) of two optical parametric generation/optical parametric amplifier (OPG/OPA) systems (Ekspra PG401SH) pumped by a same mode-locked picosecond Nd:YAG laser (Ekspra PL2143S). The two UV laser pulses, one is for pump (ν_1) and the other is for probe (ν_2), were introduced to the vacuum chamber to cross the molecular beam at right angle as a counter propagated manner. The delay time of the two laser pulses was controlled by an optical delay line. The spectral resolutions of the uv laser lights are 5 cm^{-1} . The decay profiles were analyzed by

deconvolution by assuming Gaussian shape for both pulses with the width (FWHM) of 12 ps.

The pulse width and $t = 0$ of the delay were determined by fitting the time profile of the rise of the pump-probe ion signal.

For nanosecond uv(UV) - deep uv(DUV) pump-probe spectroscopy, DUV light in the range of 198 – 230 nm was generated by sum-frequency mixing (SFM) of 1064 nm and 243 – 294 nm output with a BBO crystal: the fundamental of a YAG laser and a frequency-doubled output of a dye laser pumped by the YAG laser is overlapped on the crystal after adjusting the size and the delay of the two laser beams.³⁹ The decay profiles were analyzed by deconvolution using Gaussian shape pump and probe pulses with the width (FWHM) of 6 ns. The pulse width was determined by fitting the decay profile of the higher energy vibronic band having a lifetime shorter than 1 ns.

p-HMC (> 96% in purity) was purchased from TCI chemicals and used without further purification. *o*-HMC and *m*-HMC were synthesized by the Wittig reaction of hydroxy benzaldehyde and methyl diethylphosphonoacetate.⁴³ K_2CO_3 (3.876 g) was slowly added to a mixture of *o*-hydroxy benzaldehyde (3.43 g, 28.1 mmol) and methyl diethylphosphonoacetate (5.09 mL, 36.3 mmol) in toluene (50 mL) and refluxed at 100 °C for 5 hours. After completion of the reaction, 60% NaH was added to neutralize the solution. The crude product was washed with brine, dried with $MgSO_4$, and recrystallized in methanol to give white powdery *o*-HMC (3.90 g, 78% yield). Similarly, K_2CO_3 was added slowly to a mixture of

m-hydroxy benzaldehyde (3.43 g, 28.1 mmol) and methyl diethylphosphonoacetate (5.09 mL, 36.3 mmol) in THF (50 mL) and refluxed at 70 °C for one night. After the reaction was completed, NH₄Cl was added to neutralize the solution. The crude product was washed with water and ethyl ether, dried with MgSO₄, and recrystallized in methanol to give white powdery *m*-HMC (4.10 g, 82% yield).

2.2 Low-Temperature Matrix-Isolation FTIR Spectroscopy

The HMC powder was vaporized at 302 K and deposited with Ne gas on a CsI plate cooled by a closed-cycle helium refrigerator (Iwatani, Cryo Mini) at 6 K. Two hours were required to prepare the matrix sample. The IR spectra of the matrix-isolated samples were recorded in the range of 700–4000 cm⁻¹ using an FTIR spectrophotometer (JEOL, SPX200ST) with an accumulation number of 100. The spectral resolution was 0.5 cm⁻¹. A Xe lamp (Asahi Spectra, MAX-301uv) was used as the UV light source and was narrowed by using short-wavelength cutoff filters.

3. Theoretical calculations

3.1 Conformation search in the S₀ states

Quantum chemical calculations were performed using the *Gaussian 09* program package.⁴⁴ All conformations of the *trans*(E)-isomer were optimized under C_s symmetry, while those of the *cis*(Z)-isomer were optimized under C_s and C₁ symmetries. Several DFT approaches such as B3LYP,^{45,46} CAM-B3LYP⁴⁷ with the 6-311++G(*d*, *p*) basis set ,

M05-2X⁴⁸ with the 6-31+G(*d*) basis set and PBE0 with the cc-pVDZ basis set were tested for the electronic ground state to validate the conformational stabilities and IR spectra. The B3LYP-calculated IR spectra best reproduced the experimental ones. Therefore, we adopted the B3LYP/6-311++G(*d*, *p*) level of theory for the computational results. The obtained harmonic frequencies were scaled so that the IR frequency of the CO stretch of ester group at $\sim 1170 \text{ cm}^{-1}$ is equal to the observed one in each species. The *cis*-isomer of HMCs is $\sim 1700 \text{ cm}^{-1}$ higher in energy than the *trans*-isomer, and the barrier height for interconversion between them is higher than 10000 cm^{-1} . The relative energy as well as the energy barrier allowed us to postulate that only the *trans*-isomer is present in the sample matrix before irradiation with UV light.

3.2 Vertical ionization energy by the SAC-CI method

For identifying the final states of pump-probe spectroscopy, low-lying electronic states of the ion of HMCs were calculated using the symmetry-adapted cluster/configuration interaction (SAC-CI) method.⁴⁹⁻⁵³ The vertical ionization potentials were calculated by the direct SAC-CI non-variational (NV) method⁵⁴ in LevelFour (Lv4) accuracy.^{55,56} The 6-311G(*d*) basis set was adopted for the SAC-CI calculations. All SAC-CI calculations were carried out using *Gaussian 09*.⁴¹

3.3 Systematic search of the nonradiative decay pathways

We systematically searched NRD pathways from the $^1\pi\pi^*$ state. All calculations were

performed with the development version of the Global Reaction Route Mapping (GRRM) program interfaced with the *Gaussian 09*⁴⁴ or GAMESS 2013.1⁵⁷ quantum chemistry packages.

For *trans-o*-HMC, the minimum energy conical intersections (MECIs) between the adiabatically lowest singlet excited state (hereafter called the *S* state) and the S_0 state around the $^1\pi\pi^*$ minimum (EQs) were found by the single-component artificial force-induced reaction (SC-AFIR) method.⁵⁵⁻⁵⁷ We applied artificial forces with the model collision energy parameter $\gamma = 100$ kJ/mol. The search was initiated from the $^1\pi\pi^*$ minimum which was obtained by geometry optimization starting from the most stable ground state local minimum, and AFIR paths for fragment pairs defined for all atom pairs were computed. (See ref. 55-57 for more details of the procedure for the automated MECI search). For the *S*/ S_0 MECI search, we applied spin-flip TD-BHandHLYP theory⁶¹ for the initial search. We used the 6-31G(*d*) and 6-31G(*d,p*) basis sets for the structure search and the refinement, respectively. We obtained 56 MECIs and the ten lowest MECIs shown in Figure S1 in the Supplemental Information (SI) were further optimized using the 6-311G(*d,p*) basis set. The MECI between the $^1\pi\pi^*$ and $^1n\pi^*$ states, and the minimum energy seam of crossings (MESXs) between the $^1\pi\pi^*$ and $^3n\pi^*$ or $^3\pi\pi^*$ states nearby the $^1\pi\pi^*$ EQ were optimized at the TD- ω B97XD⁵⁹/6-311G(*d,p*) level of theory. The characters of the crossing states (*e.g.*, $\pi\pi^*$ or $n\pi^*$) were determined by checking the major configurations and the shape of the Kohn-Sham

orbitals at each MECI and MESX. The geometries of the EQs and transition states (TSs) along the decay pathways were also optimized at the (TD-) ω B97XD/6-311G(*d,p*) level of theory.

For *trans-m*-HMC, we optimized the geometries of the MECIs, MESXs, EQs, and TSs along the NRD pathways at the same level of theory as for *trans-o*-HMC. For *trans-p*-HMC, the S_0 EQ and the low-lying EQs in the T_1 state were optimized at the U ω B97XD/6-311G(*d,p*) level of theory. We constructed the initial structures for the geometry optimization of HMCs by substituting the OMe group of the corresponding optimized structure of *trans-p*-MMC, obtained in a previous study,³⁹ with the OH group. For *o*-, *m*- and *p*-HMC, we performed a normal mode analysis at all the optimized EQs and TSs to verify that the optimized structures converged to the minima or first order saddle points of the potential energy surface. The connectivity among all the optimized structures was also confirmed by calculating the intrinsic reaction coordinates (IRC) and the meta-IRC, where IRC and meta-IRC correspond to the steepest descent paths starting from the first-order saddle point and those from non-stationary points, respectively.

3.4 Rate constant of the radiative decay and spin-orbit coupling constants

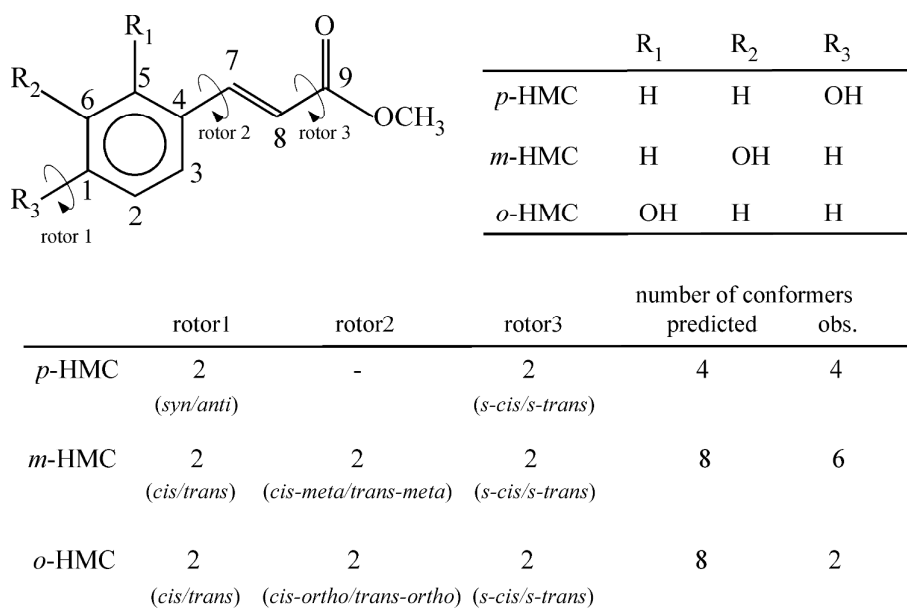
The rate constants of the radiative decay k_{rad} were estimated using Fermi's golden rule. The k_{rad} is represented as a function of the vertical emission energy $\hbar\omega$ and the oscillator strength $f(\omega)$ of the $^1\pi\pi^*$ state at the EQ,⁶³

$$k_{rad} = \frac{e\hbar\omega^3}{2\pi\epsilon_0 m_e c^3} f(\omega) \quad (1)$$

where e , ϵ_0 , m_e , and c are the elemental charge of the electron, the vacuum permittivity, the mass of the electron, and the speed of light, respectively. To evaluate the efficiency of the intersystem crossing (ISC) process, we also calculated the spin orbit coupling constants (SOCs) at the optimized MESXs using the TD- ω B97XD/6-311G(d,p) level of theory using the Breit-Pauli spin-orbit Hamiltonian with effective charge approximation,^{64,66} implemented in the PySOC program.^{67,68}

4. Results

4.1 Electronic spectra of the HMC series



Scheme 1. Molecular structures and conformations of the *trans* form of *p*-, *m*- and *o*-HMC.

Figure 1(a) shows the one-color (1C) R2PI spectrum of the S₁-S₀ transition for *p*-HMC in a supersonic beam. Buma and coworkers described the spectrum as consisting of the vibronic bands of four conformers:³¹ Here, the notations *syn* and *anti* represent the orientation of the OH group with respect to the substituent of the ring, and the notations *s-cis* and *s-trans* stand for the internal rotation of the single bond between C=C and C=O. *s*TC, *a*TC, *s*TT and *a*TT, where the first letter indicates the *anti* or *syn* orientation of the OH group (rotator1 in Scheme 1), the second one shows the *trans* or *cis* configuration of the C(8)=C(10) double bond, and the third one stands for the *s-trans* or *s-cis* configuration of the C(10)-C(12) single bond (rotator3). Figure S2 in the SI shows the structures and relative energies of the four conformers in S₀ calculated at B3LYP/6-311G(*d,p*), PBE0/cc-pVDZ, and M05-2X/6-31+G(*d*)

levels of theory. These calculations show same results for the relative energies. The energy difference between the *anti/syn* conformers is very small, while the *s-trans* conformer is ~ 300 cm^{-1} higher in energy than the *s-cis* conformer. The band at 32710 cm^{-1} consists of the (0,0) bands of the sTC/aTC conformers and similarly the band at 32880 cm^{-1} consists of the (0,0) bands of the sTT/aTT conformers.

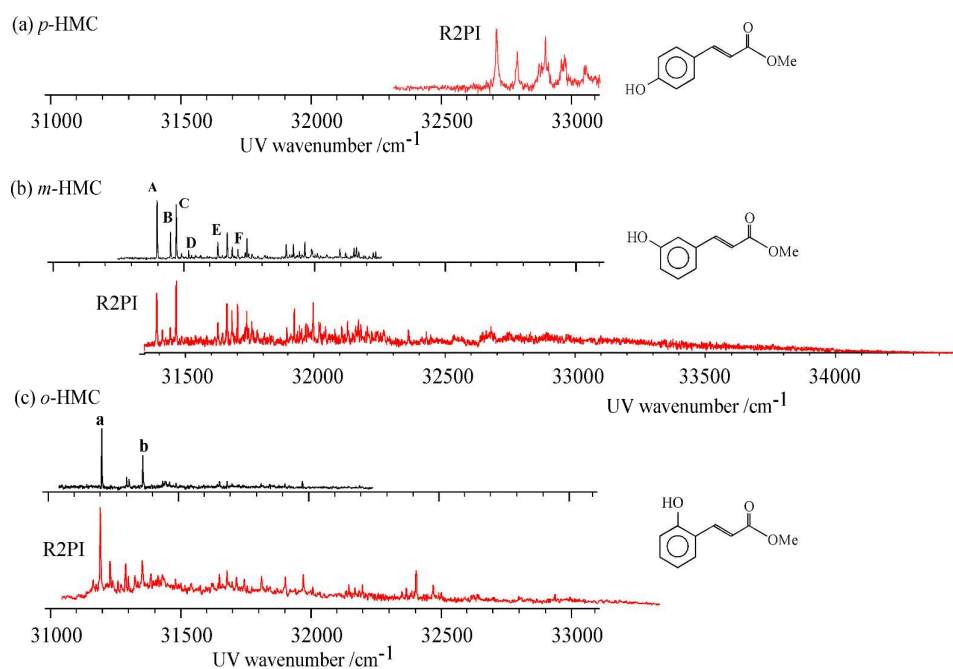


Figure 1 (a) 1C-R2PI spectrum of jet-cooled *p*-HMC. (b) LIF (upper) and 2C-R2PI (lower) spectra of jet-cooled *m*-HMC. The bands marked with capital letters are the origins of different conformers. (c) LIF (upper) and 2C-R2PI (lower) spectra of jet-cooled *o*-HMC. The bands marked with small letters are the origins of different conformers. In (b) and (c), the R2PI spectra were obtained by fixing the wavelength of the ionization laser at 225.0 nm (44440 cm^{-1}).

Figures 1(b) and (c) show the LIF (upper) and 2C-R2PI (lower) spectra of jet-cooled *m*-HMC and *o*-HMC, respectively. In the R2PI measurement, the wavelength of the

ionization laser is fixed at 225.0 nm (44440 cm^{-1}). The capital letters in (b) and the small letters in (c) indicate the coexisting conformers of *m*-HMC (Figure S3 in the SI) and *o*-HMC (Figure S4 in the SI), respectively, both revealed by the UV-UV HB spectroscopic measurements. As shown in Scheme 1, eight conformers are possible for both *m*-HMC and *o*-HMC due to the addition of the rotation along the C(3)-C(8) axis (rotator 2, Scheme 1). Thus, we add one more labeling letter to discriminate the conformers, e.g., TTTC. The structures and relative energies of the eight conformers of *m*-HMC are also shown in Figure S3. The assignment of the observed vibronic bands to these conformers is difficult because of the lack of the structural information available in an electronic/vibrational spectrum. For *o*-HMC, only two conformers are observed due to the steric hindrance between the two substituents. The S_0 stability (Figure S4) implies that these two conformers correspond to the two lowest energy conformers, TTTC and TCTC at the PBE0⁶⁶/cc-pVDZ level as well as at the B3LYP/6-311++G(*d*, *p*) and M05-2X/6-31G(*d*) levels. In addition, the calculated vertical excitation energy of TTTC is lower than that of TCTC (Figure S4), so that the species with band **a** can be assigned to TTTC and band **b** to TCTC. In the LIF and R2PI spectra, sharp vibronic bands can be identified up to $\sim 1500\text{ cm}^{-1}$ above the (0,0) band for both *m*-HMC and *o*-HMC. In the region higher than $\sim 1500\text{ cm}^{-1}$, the bands become broad and weak due to fast intramolecular vibrational energy redistribution (IVR) and NRD. Even in the R2PI spectra recorded by the nanosecond laser, the spectra show rather broad features.

4.2 S₁ lifetimes and nonradiative decay routes

4.2.1 *p*-HMC

Figure 2(a) and 2(b) shows the time profiles of the (0,0) band and the band at 32900 cm⁻¹ of *p*-HMC obtained by picosecond pump-probe spectroscopy. In this measurement, we used higher frequency for probe ionization, 39530–41150 cm⁻¹ (253.0–243.0 nm), than the previous study.³³ In the previous study, the ionization laser frequency fixed at 32590 cm⁻¹ (308.6 nm), which is ~300 cm⁻¹ higher than the IP₀. This frequency may be not high enough to ionize all the levels when IVR occurs at higher vibronic levels or to detect transient electronic states. However, as seen in the figures, only a fast decay component with a lifetime of 8 or 9 ps is observed, and no slower decay component is identified. These lifetimes are identical to the previous one.³³ The obtained lifetimes, 8 and 9 ps, are shorter than the pulse width of our picosecond laser system (12 ps), and are the upper limit which can be determined in our system. Figure 2(c) shows the time profile of *p*-HMC observed by nanosecond laser UV-DUV pump-probe spectroscopic measurement, where ν_1 is fixed at the S₁ (0,0) band and ν_2 is fixed at 50000 cm⁻¹ (200 nm). Nanosecond laser is not able to observe the fast decay (9 ps) of the S₁ state, but observe slow decay with a lifetime of 24 ns. For this molecule, Buma and coworkers also applied nanosecond pump-probe spectroscopy using 193 nm as the probe laser and observed a transient state with a lifetime of 29 ns.³⁰ They tentatively assigned this transient state to the ¹*n*π* state. However, they did not

determine the energy of this state relative to S_0 and the assignment was not definitive. Our obtained lifetime is in good agreement with their reported one so that we observe the same transient state. Figure 2(e) shows the ionization efficiency curve of this transient state and we obtained the ionization threshold at 46000 cm^{-1} . The decay time profiles of this transient state were observed at different DUV frequencies (ν_2) (See Figure S5 of SI). They show almost same decay with an average lifetime of 26 ns. Thus, it is concluded that in the picosecond laser experiment we purely measure the S_1 decay, while in the nanosecond laser experiment observes some transient state having ionization threshold of 46000 cm^{-1} and the decay lifetime of 26 ns. Then we discuss an assignment of this transient state below.

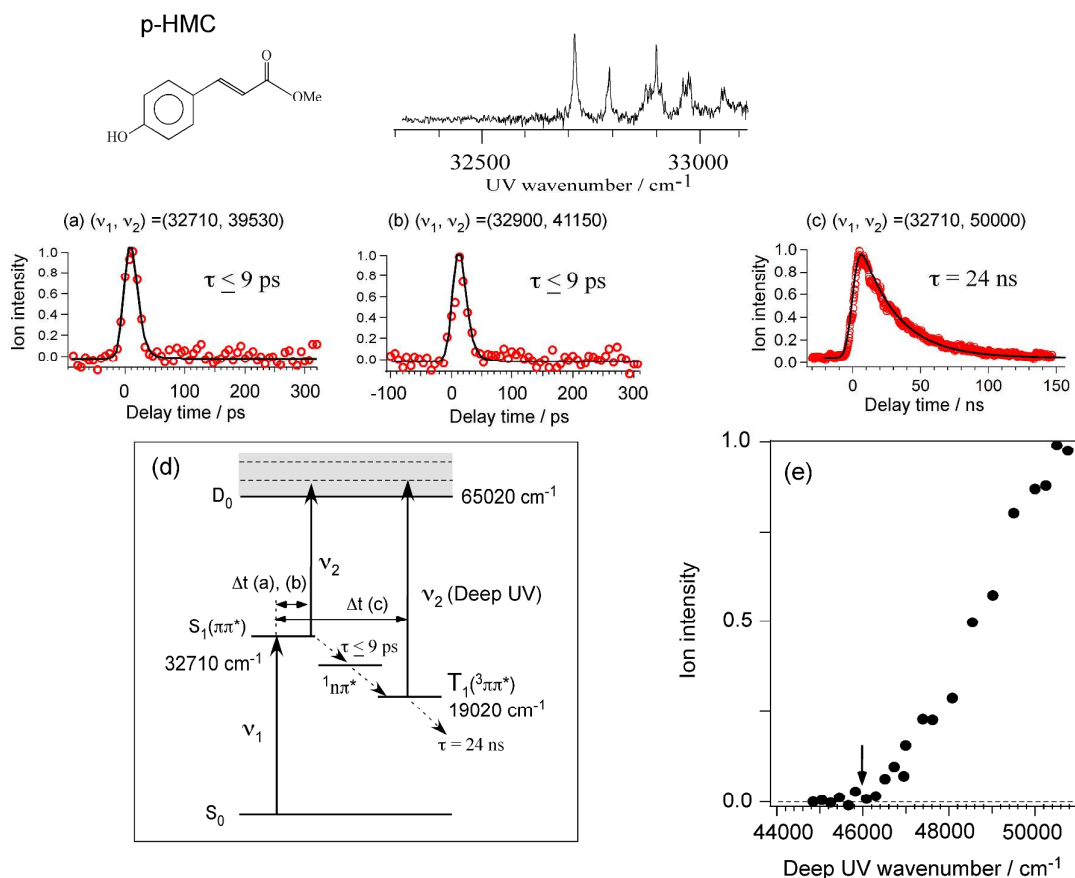


Figure 2 (a) (b) Decay profiles of S₁(0,0) band and the band at 32900 cm⁻¹ of *p*-HMC obtained by picosecond pump-probe spectroscopy. (c) Nanosecond laser UV-DUV pump-probe time profile by exciting the (0,0) band and probe laser wavelength is set at 200 nm. The profile shows a decay of the transient (T₁) state. (d) The energy level diagram, pump-probe scheme and NRD route of *p*-HMC. The ionization potential is taken from ref. 34. (e) The ionization efficiency curve by nanosecond UV-tunable DUV spectroscopy with v₁ fixed at 32710 cm⁻¹. Here v₂(DUV) is introduced at a delay time of 10 ns. The arrow indicates the ionization threshold from the T₁ state.

Figure 2(d) shows the energy levels of *p*-HMC, including S₁, ionic (D₀ and D_n) and transient states. There are two possible explanations for the observed ionization threshold: (1) ionization to the excited ionic state (D₁ or D₂) and (2) ionization to the ground ionic state (D₀). In case (1), the ionization occurs from the ¹nπ* state in accordance with the electronic configuration. Table 1 lists the vertical energies of the D₀, D₁ and D₂ states of HMC series,

obtained by DFT at ω B97XD/6-311G(*d,p*) and SAC-CI NV/6-311G(*d*) at Lv4 accuracy calculations, together with the experimentally obtained D_0 . As to D_0 s (IP_0 s), the DFT calculation shows a good agreement with the observed ones. For the energies of the excited states of ions, we adopt the values of SAC-CI method because this method is based on a multi-state theory. As seen in the table, the ionized state that is optically accessible from the $^1n\pi^*$ state is $D_2(n^{-1})$ located 13986 cm^{-1} above D_0 . The IP_0 value of *p*-HMC was reported in our previous study to be 65020 cm^{-1} .³³ From the experimental IP_0 value, the ionization threshold (46000 cm^{-1}) in Figure 2(e) and the calculated D_2 - D_0 energy gap, the energy of the $^1n\pi^*$ state is estimated to be 33000 cm^{-1} . This energy is 290 cm^{-1} higher than S_1 . In addition, as was described in the previous paper,³⁹ since the $^1n\pi^*$ state is located near the S_1 ($\pi\pi^*$) state, the two states will be strongly coupled with each other so that the $^1n\pi^*$ state should have the $^1\pi\pi^*$ character and the ionization to D_0 becomes possible, as in case (2). This leads that the energy of the transient state relative to S_0 is 19000 cm^{-1} . Such the low energy state should be the T_1 state, as described in our previous paper on *p*-MMC.³⁹ The time profiles of the transient T_1 state after exciting other vibronic bands and different probe laser wavelengths are shown in the SI (Figure S5). The T_1 state has an average lifetime of $26 (\pm 4)$ ns. Thus, similar to *p*-MMC, we conclude that the [$S_1 \rightarrow ^1n\pi^* \rightarrow T_1$] NRD process occurs in *p*-HMC in a timescale of less than a few nanoseconds, and the T_1 state decays with a lifetime of 26 ns.

As was described above, we could not detect the $^1n\pi^*$ state of *p*-HMC by picosecond

pump-probe spectroscopy using a higher probe laser frequency. This indicates either that the lifetime of the transient $^1n\pi^*$ state is very short or that the probe laser frequency (41670 cm^{-1}), which is the shortest UV frequency we can generate with the present picosecond laser system), is still not high enough to ionize the state.

Table 1. Vertical ionization energies (cm^{-1}) of the selected excited states of *p*-, *m*- and *o*-HMC calculated using the ω B97XD/6-311G(*d,p*) and SAC-CI NV/6-311G(*d*) at Lv4 accuracy.

Method	State	<i>p</i> -HMC	<i>m</i> -HMC	<i>o</i> -HMC
DFT				
(ω B97XD/ 6-311G(<i>d,p</i>))	$D_0(\pi^{-1})$	65007	67229	65912
SAC-CI				
(NV/6-311G(<i>d</i>), Lv4)	$D_0(\pi^{-1})$	61516	64194	62597
	$D_1(\pi^{-1})$	74066 (12550 ^a)	68138 (3944 ^a)	69339 (6742 ^a)
	$D_2(n^{-1})$	75502 (13986 ^a)	76429 (12235 ^a)	74695 (12013 ^a)
Experiment	$D_0(\pi^{-1})$	65020 ^b	67623 ^c	66165 ^c

a) Relative energy from D_0

b) Ref. 33.

c) This work.

4.2.2 *m*-HMC and *o*-HMC

Before the lifetime measurements, the ionization potentials (IP_0) were determined for *m*-HMC and *o*-HMC. Figures 3(a) and (b) show the ionization efficiency curves of *m*-HMC and *o*-HMC from the zero-point energy level of S_1 , respectively, by the nanosecond pump-probe experiment. For *m*-HMC, ν_1 is fixed at 31393 cm^{-1} and the ionization threshold is recorded at $\nu_2 = 36230\text{ cm}^{-1}$, which gives 67623 cm^{-1} for IP_0 . For *o*-HMC, ν_1 is fixed at 31195 cm^{-1} and the ionization threshold is recorded at $\nu_2 = 34970\text{ cm}^{-1}$, giving $IP_0 = 66165\text{ cm}^{-1}$. Therefore, both molecules have S_1 zero-point energies that are less than half of the IP_0 . Thus to carry out the pump-probe experiment the probe frequency must be higher than the pump frequency. The obtained IP_0 values are also listed in Table 1 and are compared with the vertical ionization potentials calculated by the DFT and SAC-CI method. The DFT calculated IP_0 s show excellent agreement with the observed ones.

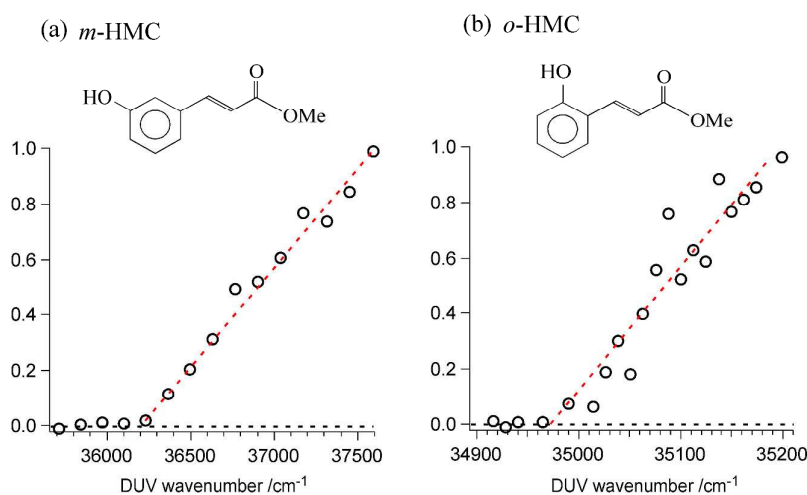


Figure 3 Ionization efficiency curve of (a) *m*-HMC from the zero-point vibrational energy level of S_1 for isomer A (band A, 31393 cm^{-1}), and (b) *o*-HMC from the zero-point vibrational energy level of S_1 for isomer a (band a, 31195 cm^{-1}). From the thresholds, the IP_0 is determined to be 67623 cm^{-1} for

m-HMC and 66165 cm^{-1} for *o*-HMC.

The lower left panel of Figure 4 shows the time profiles of the vibronic bands of S_1 for *m*-HMC observed by nanosecond UV(ν_1)-UV'(ν_2) and UV(ν_1)-DUV(ν_2) pump-probe spectroscopy. Figures 4(a) and (b) show the time profile of (0,0) band with the probe wavelength of 270 nm ($\nu_2 = 37040\text{ cm}^{-1}$) and 202 nm (DUV), respectively. The two decay curves are almost identical and can be fitted by a single exponential decay curve with a lifetime of 10 ns. Thus, in both experiments we observe purely a decay of the S_1 state. Figure 4(c) shows a decay profile of band (f) located at 700 cm^{-1} above (0,0) band showing a decay lifetime of 6 ns. Figure 4(d) shows a decay profile of band (h) located at 2100 cm^{-1} . The profile shows very fast decay whose lifetime is too fast to be determined by the nanosecond laser. In addition, different from *p*-HMC it does not exhibit long lifetime component attributed to T_1 even if we use DUV as a probe laser light (ν_2). This suggests that in *m*-HMC the T_1 state is not generated in the nonradiative decay process. Lower right panel of Figure 4 shows typical decay profile of the higher vibronic levels observed by picosecond pump-probe experiment with $\nu_2 = 41150\text{ cm}^{-1}$ (243 nm). This ionization energy is high enough to ionize the pumped levels as well as the IVR redistributed levels in S_1 . All the decay profiles can be fitted by single exponential decay curves. The decay profiles of all the labeled bands in the R2PI spectrum of Figure 4 are shown in the supplement information (Figure S6).

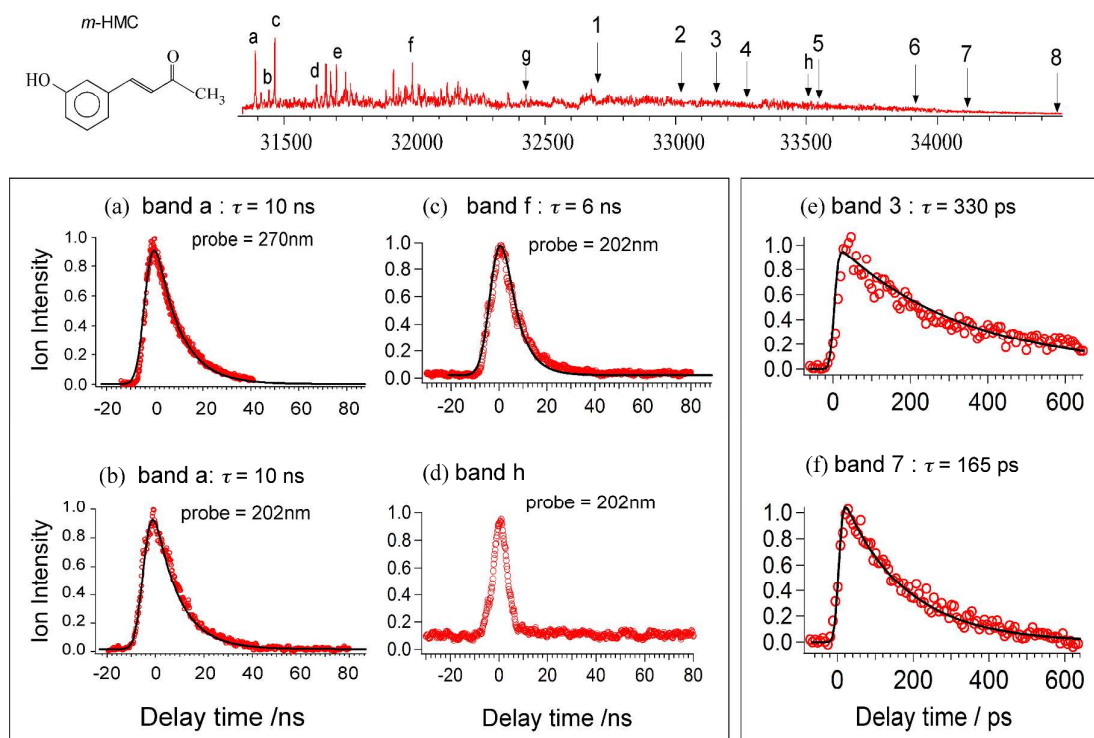


Figure 4. (Upper panel) 2C-R2PI spectrum of *m*-HMC. (Lower panel) (left)(a),(b) Time profile of the (0,0) band by the nanosecond pump-probe experiment with different probe laser wavelengths. (c),(d) Time profile of bands (c) and (h) with 202 nm probe. (right)(e),(f) Time profiles of vibronic bands by picosecond pump-probe experiment with 243 nm probe. Solid curves are convoluted decay curves with single exponential decay. Time profiles of other vibronic bands are shown in Supplement Information (Fig. S6).

Similar measurements have been carried out for *o*-HMC. Figures 5(a) and (b) are the time profiles obtained by the nanosecond pump-probe experiment with the probe laser wavelength fixed at 202 nm. The S_1 lifetimes of the vibronic bands of *o*-HMC are shorter than those of *m*-HMC, so that only the lifetime of the zero point level is obtained with the nanosecond laser experiment. Similar to the case of *m*-HMC, we do not find a long lifetime transient state attributed to T_1 even by exciting band **b** at 33430 cm^{-1} ($(0,0) + 2217\text{ cm}^{-1}$) as seen in Figure 5(b). The ion signal is attributed to the DUV ionization of the S_1 state, the

lifetime of which is too fast to be determined by the nanosecond laser ionization scheme. Figures 5(c)-(e) show the time profiles of vibronic bands by picosecond pump-probe experiment with 243 nm probe. Similar to *m*-HMC, all the decay profiles are fitted by single exponential decay curves. The time profiles of the labeled vibronic bands in the R2PI spectrum in upper panel of Figure 5 are shown in the supplement information (Figure S7).

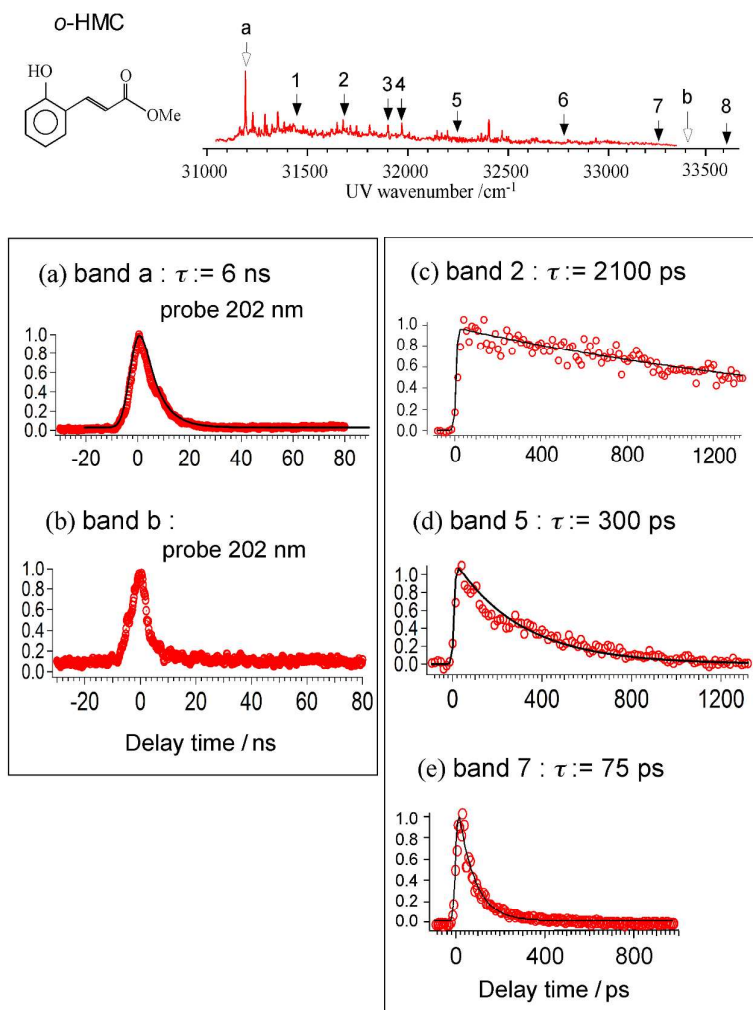


Figure 5 (Upper) 2C-R2PI spectrum of *m*-HMC. (Lower) (a),(b) Time profiles of the (0,0) band and band (b), respectively, of *m*-HMC by the nanosecond UV-DUV pump-probe experiment (c–e) Time profiles obtained by picosecond UV-UV' pump-probe experiment (c–e). Solid curves are the fits to single exponential decay curves. Time profiles of other vibronic bands are shown in Supplement Information (Fig. S7).

Figures 6(a) and (b) show the plots of the decay rate constant (k) versus the excitation (and excess) energy for *o*-HMC and *m*-HMC, respectively. It should be noted that the decay rate constants of *o*-HMC and *m*-HMC are much smaller than *p*-HMC even at an excess energy of 2500–3000 cm⁻¹. The S₁ decay rate constant of *p*-HMC is 1.1×10^{11} s⁻¹, even at the zero-point level. In *m*-HMC, the decay rate constant shows a remarkable increase at

$E_{\text{excess}} = \sim 1000 \text{ cm}^{-1}$, indicating an opening of the NRD channel. In *o*-HMC, a similar onset is seen at $E_{\text{excess}} = \sim 600 \text{ cm}^{-1}$. It should also be noted that IVR may occur at high energy and its effect on the decay profile will be discussed later.

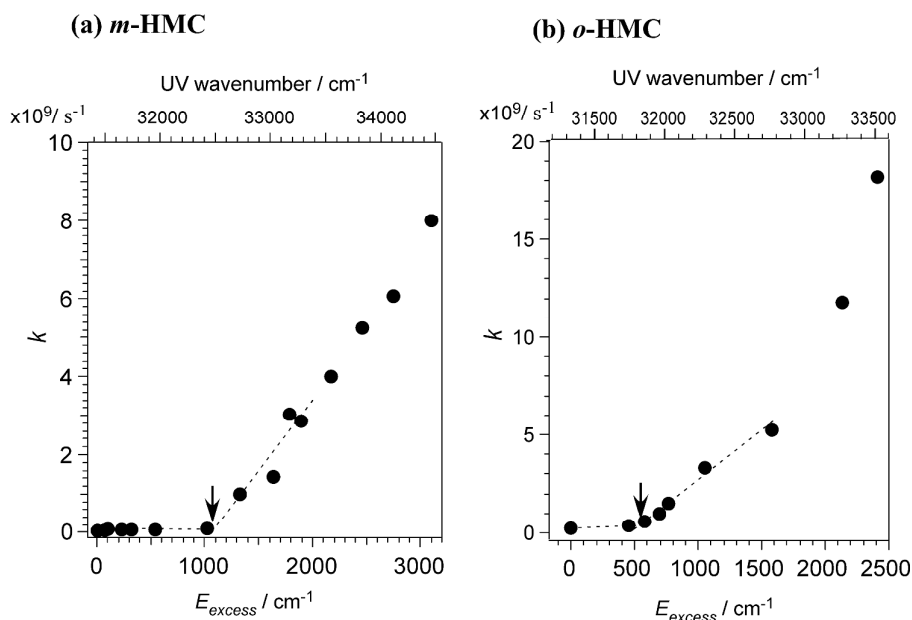


Figure 6 Plots of the decay rate constants of (a) *m*-HMC and (b) *o*-HMC as a function of excess energy.

4.3 Matrix-isolated FTIR experiment

4.3.1 *p*-HMC

Figure 7(a) shows the FTIR spectrum of matrix-isolated *p*-HMC before UV irradiation. The IR spectrum exhibits a strong peak at 1174 cm^{-1} and other relatively weak peaks. To reproduce the observed spectrum, the conformational stabilities and IR intensities were analyzed by comparison with DFT calculations. The calculated structures and relative energies at the B3LYP/6-311++G(*d,p*), PBE0/cc-pVDZ, and M05-2X/6-31+G(*d*) levels are

shown in Figure S2 in the SI. The vibrational frequencies are scaled a factor of 0.9941 to fit the observed IR band of the CO stretch of ester group at 1171 cm^{-1} . Figures 7(b) and (c) are the calculated IR spectra of the *s-cis* and *s-trans* conformers, respectively. The red and blue lines indicate *anti* and *syn*, respectively, giving almost identical IR spectra. In addition, their stability is not distinguishable. Therefore, we will not discuss differences in the *s-cis/s-trans* conformers. By comparison with the calculated spectra, the sharp band appearing at 1174 cm^{-1} can be assigned to the ester C-O stretching mode. The absorption intensity implies that the *s-cis* conformer is more populated than the *s-trans* conformer. In fact, the sum of the calculated spectra of the conformers is best reproduced by the Boltzmann distribution of the vaporized temperature and the conformational stability as shown in Figure 7(d).

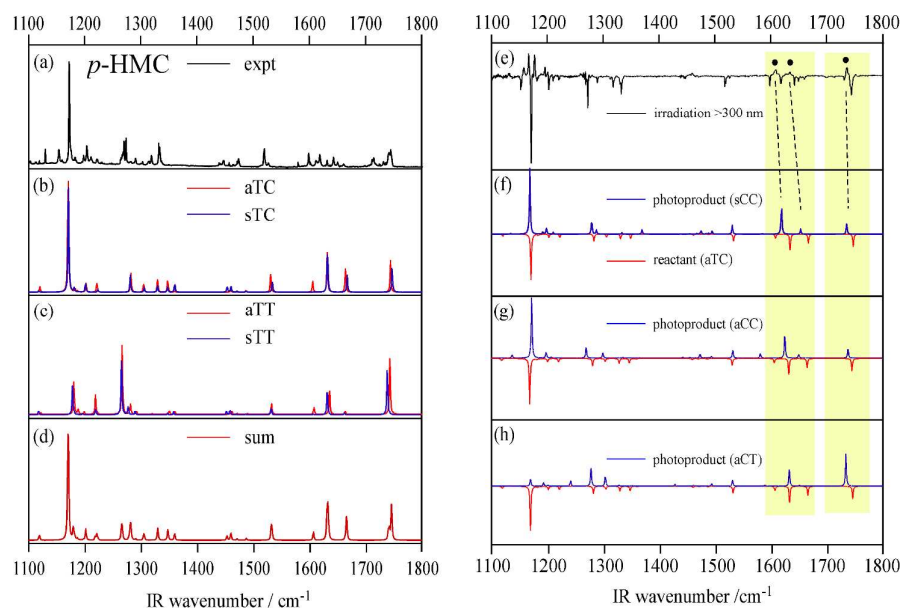


Figure 7 (a) FTIR spectrum of matrix-isolated *p*-HMC. (b)(c) Calculated IR spectra of four conformers of *p*-HMC at the B3LYP/6-311++G(*d*, *p*) level of DFT. (d) Calculated IR spectrum obtained by combining the four conformers assuming a Boltzmann distribution at the vaporized temperature (302 K). The calculated vibrational frequencies are scaled by a factor of 0.9941. (e)

Difference FTIR spectra of the matrix-isolated *p*-HMC before and after UV irradiation at $\lambda_{UV} \geq 300$ nm. Positive peaks are due to the product and negative ones are depletion of the reactant. (f)–(h) Comparison of the IR spectra of the *cis*-products (blue) and the *trans*-reactants (red). The dotted bands are typical bands of the *cis*-products.

Figure 7(e) shows the difference FTIR spectrum of *p*-HMC before and after UV irradiation at $\lambda_{UV} \geq 300$ nm. The positive absorption indicates the photoproduct and the negative one is the depleted population of the initial reactant. For simplicity, the most stable aTC conformer is considered to be the initial reactant. Figures 7(f) and (h) display the comparison of the IR spectra assuming that the *trans* \rightarrow *cis* isomerization occurs from the aTC reactant to the sCC, aCC and aCT products, respectively. The structures and energies of the optimized *cis*-isomers obtained at the B3LYP/6-311G(*d*, *p*) level of theory are shown in the SI (Figure S8). Since B3LYP does not include interaction, the magnitude of the relative energies might be affected upon the inclusion of dispersion force especially aTC and sTC conformers. However, the energies of the two conformers are very high so that the order of the relative energies might not change. Typical vibrations indicating the production of the *cis*-isomer, such as propenyl C=C stretching at ~ 1630 cm^{-1} and C=O stretching at ~ 1740 cm^{-1} , are highlighted in the spectra. In addition, the ring C-C stretching vibration at ~ 1610 cm^{-1} shows a typical shift in the *cis*-isomer. The possibility of a *s-cis* \rightarrow *s-trans* conformational change within the *trans*-configuration, such as aTC or sTC, can be ruled out due to poor agreement with the observed difference spectrum. Therefore, it is clear that the *trans* \rightarrow *cis*

isomerization occurs in *p*-HMC upon the UV irradiation, which is essentially the same reported previously for *p*-MMC.³⁵

4.3.2 *m*-HMC

Figure 8(a) shows the matrix-isolated FTIR spectrum of *m*-HMC. Figures 8(b)–(d) are the IR spectra of the possible abundant conformers obtained by B3LYP/6-311++G (*d, p*) calculations. The vibrational frequencies are scaled a factor of 0.9927 to fit the observed IR band of the CO stretch of ester group at 1176 cm⁻¹. The experimental spectrum is reproduced by adding the calculated spectra of the conformers and considering the Boltzmann distribution of the vaporized temperature (302 K), as shown in Figure 8(f). The calculated spectra show reasonable agreement with the observed one. We first irradiated UV light at $\lambda_{UV} \geq 320$ nm, near the (0,0) band, to observe the product. However, since vibration due to the photoproduct was observed, the photochemical reaction does not occur at this wavelength. Figure 8(g) shows the difference IR spectrum of *m*-HMC before and after UV irradiation at $\lambda_{UV} \geq 300$ nm, where several new bands due to the photoproduct appear. To identify the photoproducts, we considered the *cis*-product. From the calculated *cis*-isomer structures and their relative stabilities (Figure S9 in the SI), the CCCC conformer is most stable. Similar to *p*-HMC, the functional used in the calculation does not have a dispersion interaction and the magnitude of the relative energies might be affected upon the inclusion of dispersion force, especially for TTCT, CTCT, TCCT, and CCCT conformers. However, the

energies of these conformers are very high so that the order of the relative energies might not change. Hence, this conformer was selected as the major photoproduct and we compared the simulated IR spectrum of the CCCC conformer with those of the initial *trans*-*m*-HMC as seen in Figures 8(h)–(k). Although the assumption of the production of one conformer (CCCC) is very simple, it is clear that the newly appearing peaks, such as the bands at 1635 cm^{-1} (propenyl C=C stretching band) and 1740 cm^{-1} (C=O stretching), can be assigned to the *cis*-product. Thus, we conclude that the *trans* \rightarrow *cis* isomerization occurs by UV irradiation of *trans*-*m*-HMC.

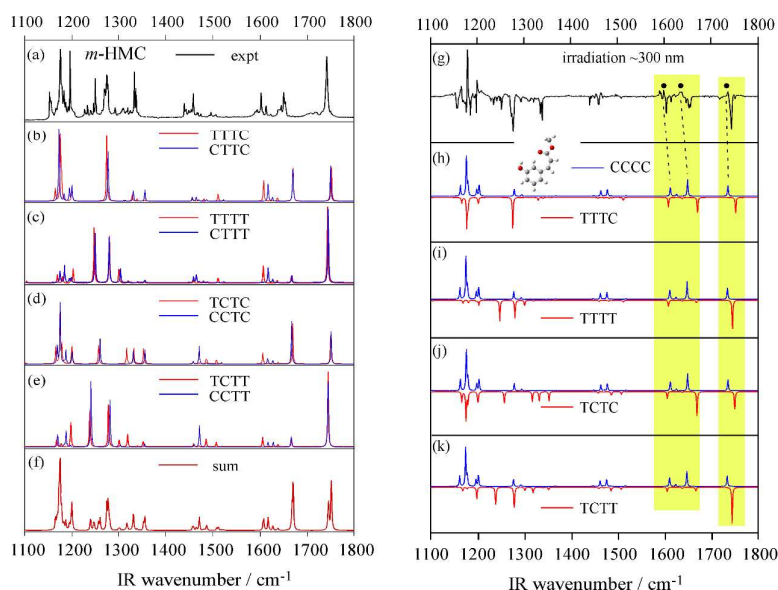


Figure 8 (a) FTIR spectrum of matrix-isolated *m*-HMC before UV irradiation. (b)–(e) Calculated IR spectra of TTTC, TTTT, TCTC and TCTT, respectively, at the B3LYP/6-311++G(*d*, *p*) level. The red and blue spectra indicate OH-*trans* and OH-*cis*, respectively. (f) The sum of the calculated spectra using the Boltzmann distribution at the vaporizing temperature and relative energies. The vibrational frequencies are scaled by a factor of 0.9927. (g) Difference IR spectrum of matrix-isolated *m*-HMC before and after UV irradiation at $\lambda_{UV} \geq 300\text{ nm}$. (h)–(k) Comparison of the difference IR spectra of the CCCC conformer of the *cis*-product and various conformers of *trans*-*m*-HMC. The dotted bands

are typical bands of the *cis*-products.

4.3.3 *o*-HMC

Figure 9(a) shows the matrix-isolated FTIR spectrum of *o*-HMC. Similar to the treatment discussed above, the experimental spectrum is reproduced by the sum of the calculated spectra of the conformers in Figures 9(b) and (c) by considering the Boltzmann distribution of the vaporized temperature and relative energies of the conformers, which are shown in Figure S4 in the SI. The vibrational frequencies are scaled a factor of 0.9926 to fit the observed IR band of the CO stretch of ester group at 1171 cm^{-1} . The resultant spectrum of *o*-HMC in Figure 9(f) reasonably reproduces the observed one in Figure 9(a). Figure 9(g) shows the difference IR spectrum of *o*-HMC before and after UV irradiation at $\lambda_{\text{UV}} \geq 300\text{ nm}$. Similar to the case of *m*-HMC, we did not observe the product by $\lambda_{\text{UV}} \geq 320\text{ nm}$ excitation. In Figure 9(g), we see several new bands (marked by dots) from the photoproduct, which may be *cis-o*-HMC.

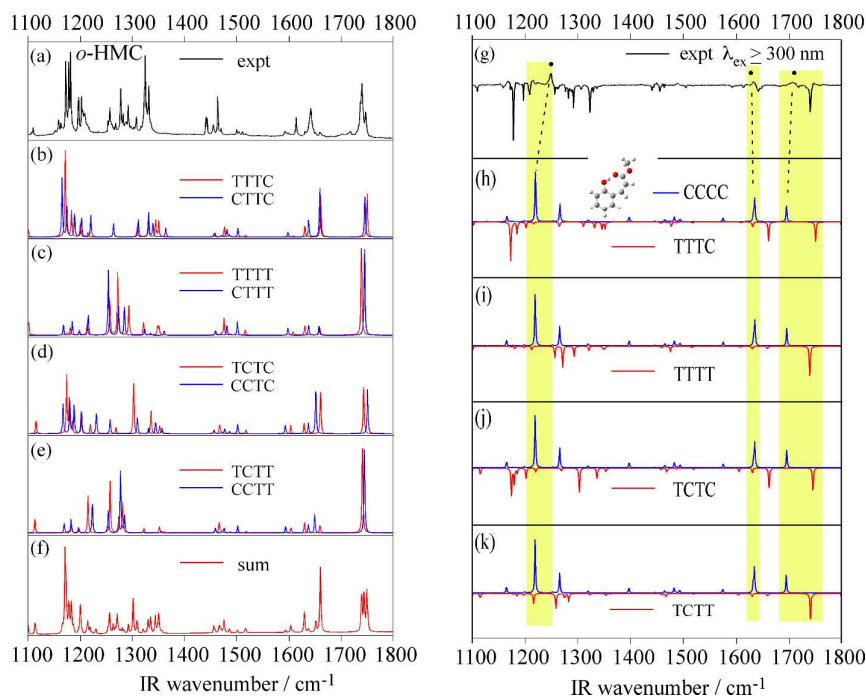


Figure 9 (a) FTIR spectrum of matrix-isolated *o*-HMC before UV irradiation. (b)–(e) Calculated IR spectra of TTTC, TTTT, TCTC and TCTT, respectively, at the B3LYP/6-311++G(*d*, *p*) level. The red and blue spectra indicate OH-*trans* and OH-*cis*, respectively. (f) The sum of the calculated spectra using the Boltzmann distribution at the vaporizing temperature (302 K) and relative energies for conformers. The vibrational frequencies are scaled by a factor of 0.9926. (g) Difference IR spectrum of matrix-isolated *o*-HMC after UV irradiation at $\lambda_{UV} \geq 300$ nm. (h)–(k) Comparison of the IR spectra of the CCCC conformer of the *cis*-product and various conformers of *trans*-*o*-HMC. The dotted bands are typical bands of the *cis*-products.

The calculated possible structures of the *cis*-product are compared with the difference IR spectra in the right part of Figure 9. The calculated structures and the energies of the *cis*-product are shown in Figure S10 in the SI. Among the possible structures, the CCCC conformer is most stable, so that we consider this conformer to be the major product. The CCCC conformer is stabilized by hydrogen-bonding between the OH group at the *ortho*-position and the C=O of the ester group. We compared the IR spectrum of the CCCC conformer with those of several conformers of *trans*-*o*-HMC, as seen in Figures 9(h)–(k).

Among three noticeable peaks of the product, the observed peak at 1633 cm^{-1} is assigned to the propenyl C=C stretching mode. In addition, the C=O stretching band at 1710 cm^{-1} is well reproduced in the calculated spectrum of the CCCC conformer. Therefore, we also conclude that *trans* \rightarrow *cis* isomerization occurs in *trans-o*-HMC upon UV irradiation.

5. Discussion

5.1 Nonradiative decay route leading to the *trans* \rightarrow *cis* isomerization

5.1.1 *p*-HMC

The experimental results for *p*-HMC indicate that the NRD route from S_1 to the *cis*-product is essentially the same as those of *p*-MMC and *para*-methoxy-ethylcinnamate (*p*-MEC), reported previously.³⁴ We concluded that the NRD route is [$S_1 \rightarrow {}^1n\pi^* (\rightarrow T_2) \rightarrow T_1 (\pi\pi^*)$] in both species. The initial $S_1 \rightarrow {}^1n\pi^*$ IC decay proceeds with lifetimes shorter than 1 ns in these molecules. The next ${}^1n\pi^* (\rightarrow T_2) \rightarrow T_1$ steps are also very fast because the nanosecond UV-DUV pump-probe experiment can only detect the T_1 state. Since the S_1 lifetime of *p*-HMC is more than 10 times shorter than those of *p*-MMC and *p*-MEC, the ${}^1n\pi^*$ potential energy curve is thought to cross nearly at the bottom of that of S_1 in *p*-HMC, leading to barrier-less IC. In *p*-MMC and *p*-MEC, TDDFT calculations predicted that the T_1 state has a structure that is twisted along the propenyl C=C bond by $\sim 95^\circ$.³⁴ The energy of the T_1 state from S_0 was obtained experimentally to be 16577 and 17024 cm^{-1} for *p*-MMC and *p*-MEC,

respectively.³⁴ In the present study, the energy of the T_1 state of *p*-HMC was experimentally determined to be 19020 cm^{-1} , and the T_1 state molecule relaxes to either the *trans*- or *cis*-form of S_0 with a lifetime of $26 \pm 2\text{ ns}$ (See Figure S5 in the SI).

Since the NRD route of *p*-HMC³⁵ is essentially the same as those of *p*-MMC^{34,39} and *p*-MEC³⁹, we calculated only the energy and the structure of the T_1 state to confirm that the observed transient state in *p*-HMC is also the T_1 state. We searched for the stable conformers of T_1 using $U\omega B97XD/6-311G(d, p)$ calculations. We found two C=C twisted conformers, *p*-EQ1 and *p*-EQ2, in T_1 as shown in Figure 10. The C=C torsional angle ϕ is 91° in *p*-EQ1 and 89° in *p*-EQ2. The calculated transition energy from the *trans* conformer of the S_0 state is 17900 cm^{-1} for *p*-EQ1 and 17804 cm^{-1} for *p*-EQ2, both of which agree with the experimental value of 19020 cm^{-1} . The calculated energy difference between *p*-EQ1 and *p*-EQ2 is only 96 cm^{-1} . Hence, there is an equilibrium between the two conformers and they co-exist with a ratio of *p*-EQ1:*p*-EQ2 $\approx 4:5$, assuming a Boltzmann distribution at 580 K, which corresponds to the excess energy in the T_1 state. These features are very similar to those of *p*-MMC and *p*-MEC.³⁹

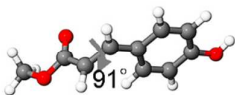
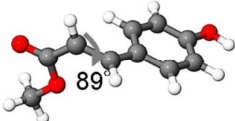
EQ	Structure	Energy / cm^{-1}
<i>p</i> -EQ 1		17900
<i>p</i> -EQ 2		17804
Exp.	-----	19020

Figure 10 The optimized structures and (0,0) transition energies of *p*-HMC in the T₁ state. The results are from the UωB97XD/6-311G(*d,p*) level of theory.

5.1.2. *m*-HMC and *o*-HMC

In contrast to *p*-HMC, the decay lifetimes of the S₁ state of *m*-HMC and *o*-HMC are 1000 times slower at the zero-point level. This can be understood by considering that the potential crossing between S₁ and the excited electronic state leading to the NRD channel, such as the ¹*nπ** state, occurs at higher energies in *m*-HMC and *o*-HMC than in *p*-HMC. The plots of the decay rate constants vs. the energy in Figure 6 indicate that the opening of the NRD channel occurs at ~1000 cm⁻¹ in *m*-HMC and ~600 cm⁻¹ in *o*-HMC. As discussed above, this is in accordance with the low temperature matrix experiment, in which excitation by λ_{UV} ≥ 320 nm (near the (0,0) band) does not produce the *cis*-product in *m*-HMC and *o*-HMC, and an excess energy of 2000 cm⁻¹ (300 nm) at the maximum is necessary to promote effective photoisomerization. Another important difference between *m*-HMC/*o*-HMC and *p*-HMC is that we did not observe the T₁ transient state in *m*-HMC and *o*-HMC even at an excess energy of ~2200 cm⁻¹ in the S₁ state. This suggests that in *m*-HMC and *o*-HMC the T₁ state is not a precursor of the *cis*-photoproduct and the isomerization proceeds via a different route.

Before calculating the NRD route, we first discuss the effect of IVR on the decay profiles of the S₁ state. We found that all the decay curves of the S₁ vibronic levels showed single exponential decay curves in both *m*-HMC and *o*-HMC. It is possible that IVR

competes with NRD at higher vibronic levels, although it is not clear at what energy the IVR will occur and compete with NRD. If IVR is faster than NRD, the decay curve might exhibit double exponential decay because of the difference in the NRD rate between the initially pumped level and the IVR redistributed levels. The observed single exponential decay suggests that NRD is faster than IVR in both molecules.

We next focus on the observed excess energy dependence of the decay rate constant of *m*-HMC and *o*-HMC based on the theoretical results of NRD pathways. We experimentally found that the major decay route of the S_1 ($^1\pi\pi^*$) state turns from the radiative into nonradiative at a threshold energy of ~ 1000 cm^{-1} for *m*-HMC and ~ 600 cm^{-1} for *o*-HMC, and above these energies the decay rate constant of the $^1\pi\pi^*$ state linearly increases with the excess energy. The calculated radiative lifetime $\tau_{\text{rad}} = 1/k_{\text{rad}}$ at the TD- ω B97XD/6-311G(*d,p*) (present work) and SAC-CI/D95(*d*) level of theory²⁸ are summarized in Table 2. These calculated values agree with the experimental ones both for *m*-HMC and *o*-HMC. Thus, we conclude that below the threshold, the $^1\pi\pi^*$ state undergoes radiative decay.

Table 2 Comparison between the theoretical and experimental radiative lifetimes τ_{rad} of the $^1\pi\pi^*$ state of *m*-HMC and *o*-HMC (in ns).

Molecule	TD- ω B97XD/ 6-311G(<i>d,p</i>) ^a	SAC-CI/ D95(<i>d</i>) ^b	Exp. ^a
<i>m</i> -HMC	4.5	6.2	10
<i>o</i> -HMC	2.7	4.4	6

^a Present work

^b M. Promkatkaew *et al.*²⁸

Above this threshold, the NRD pathway becomes accessible. We examined several NRD routes: (1) NRD to $^1n\pi^*$ via the S_1 ($^1\pi\pi^*$)/ $^1n\pi^*$ MECI followed by $^1n\pi^* \rightarrow T_n$ ISC, (2) ISC from S_1 to $^3n\pi^*$ or $^3\pi\pi^*$, and (3) structural change along the C=C twisted coordinate on the S_1 surface followed by IC to S_0 via $^1\pi\pi^*/S_0$ MECI1 which triggers *trans* \rightarrow *cis* isomerization.²⁸ We concluded that route (3) is the most likely, as shown in Figure 11. In Figure 11(a), the activation barrier of TS1 is located at $\phi \sim 135^\circ$, connecting the energy minimum of the *trans* isomer in the S_1 ($^1\pi\pi^*$) states and MECI 1 ($^1\pi\pi^*/S_0$), the barrier height of which is calculated to be 1258 cm^{-1} for *m*-HMC. For *o*-HMC in Figure 11(b), the barrier is calculated to be 649 cm^{-1} . In both cases, a zero-point energy correction is included. These values are close to the experimentally obtained threshold energies of the lifetime shortening: $\sim 1000 \text{ cm}^{-1}$ for *m*-HMC and $\sim 600 \text{ cm}^{-1}$ for *o*-HMC. After the *trans* \rightarrow *cis* isomerization in S_0 ,⁷⁰ further conformational change to the most stable CCCC conformer (see Figure 11(a) and (b)) will occur due to the large excess energy and trivial activation barriers.

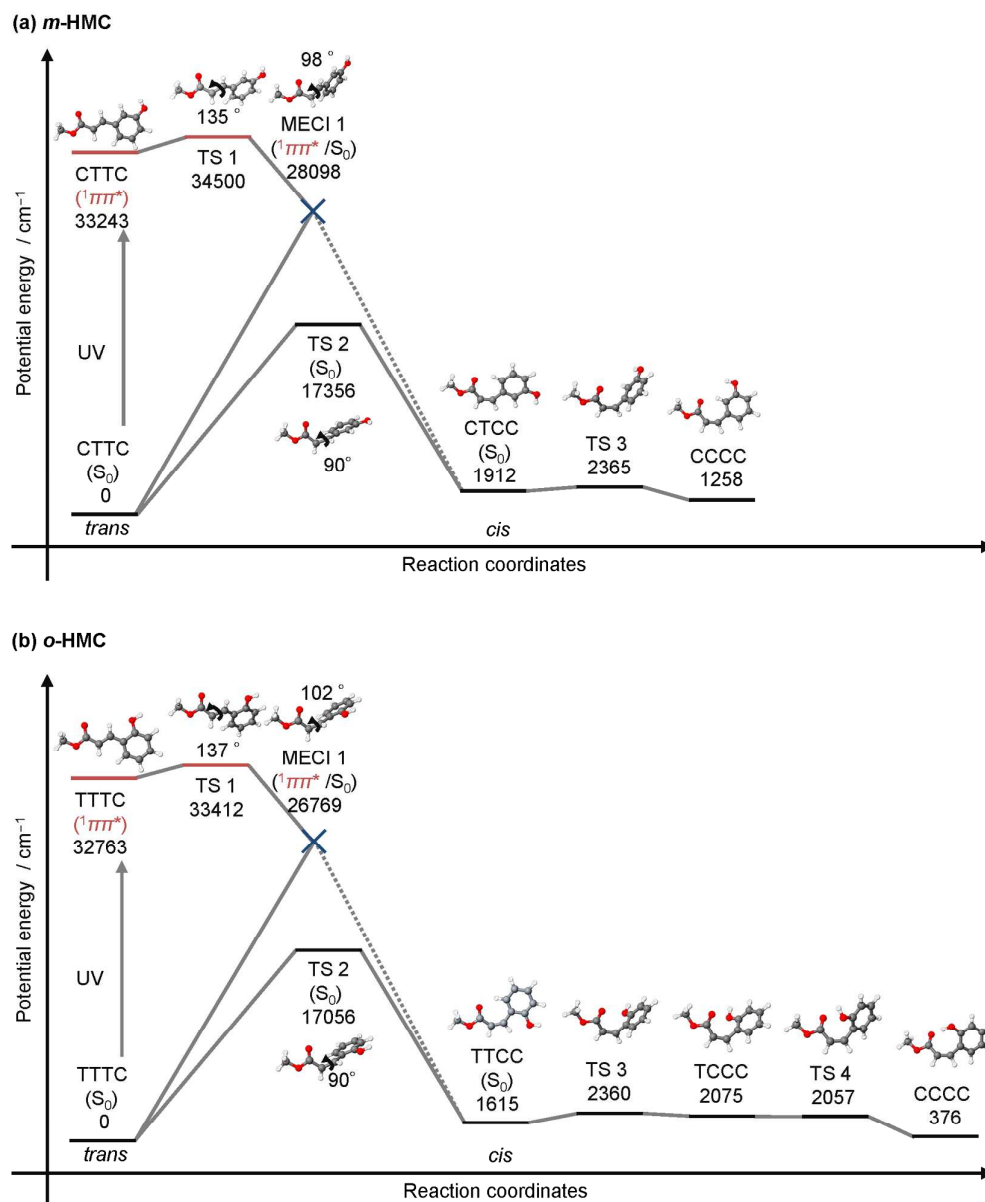


Figure 11 Potential energy profiles from the photoexcited *trans*-HMC to the *cis*-product and the subsequent conformational change in (a) *m*-HMC and (b) *o*-HMC. The EQs and TSs are optimized at the (TD-)(U) ω B97XD/6-311G(*d,p*) level of theory. Zero-point energy corrections are included to calculate the relative potential energies. MECI 1 was optimized at the spin-flip TD-BHandHLYP/6-311G(*d,p*) level of theory. Zero-point energy corrections were not included to calculate the relative potential energies of MECI1.

We also theoretically investigated the other two NRD routes: (route 1) IC to the $^1n\pi^*$ state followed by ISC to triplet states and (route 2) direct ISC to triplet states, and concluded

that neither of them contributes significantly to the NRD process. We listed the energies of the several low lying electronic states which will be involved in NRD calculated by TD- ω B97XD/6-311G(*d,p*) level of theory in Table S1 in the SI. Figure 12 summarizes the relative energies of the MECI and MESX near the ${}^1\pi\pi^*$ minimum of the *trans* forms of *m*-HMC and *o*-HMC. The IC to the ${}^1n\pi^*$ state is energetically unfavorable. The energy of ${}^1n\pi^*$ (EQ3) is 935 and 1517 cm^{-1} higher than ${}^1\pi\pi^*$ EQ1 in *m*-HMC and *o*-HMC, respectively. Accordingly, ${}^1\pi\pi^*/{}^1n\pi^*$ MECI2 is located at 1695 cm^{-1} in *m*-HMC and 1988 cm^{-1} in *o*-HMC. Both are energetically higher than the C=C rotation energy barrier.

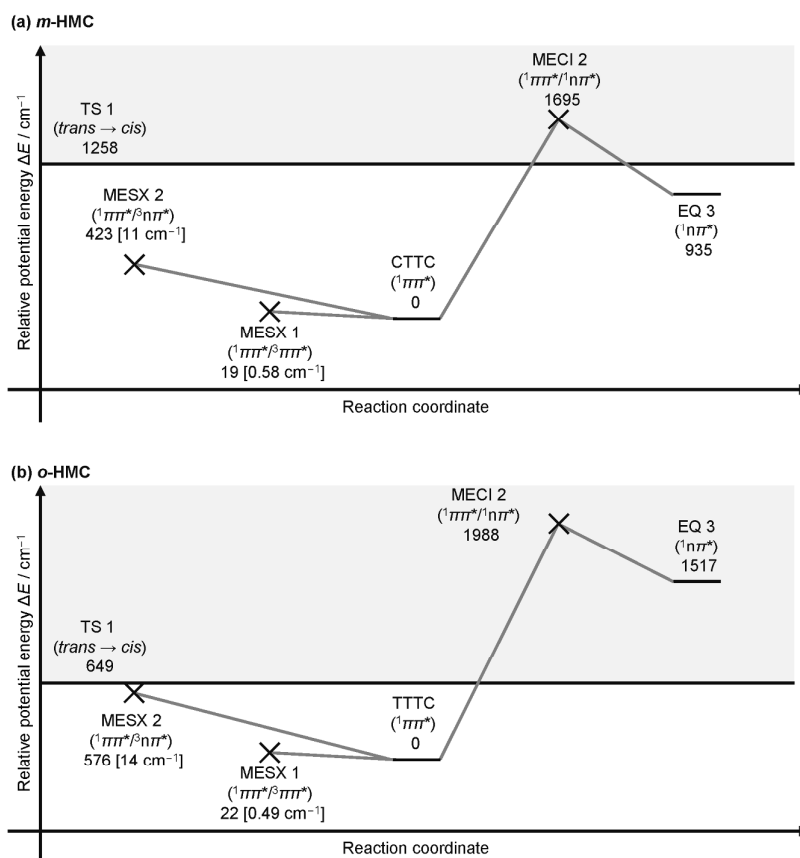


Figure 12. Potential energy profile of IC to the ${}^1n\pi^*$, and ISC to triplet states from the ${}^1\pi\pi^*$ states; (a) *m*-HMC and (b) *o*-HMC. All the structures were optimized at the TD- ω B97XD/6-311G(*d,p*) level of

theory. Zero-point energy corrections are included to calculate the relative potential energies of EQs and TS but not MECI and MESX. The calculated values of the $|\text{SOC}|$ at the TD- $\omega\text{B97XD}/6\text{-311G}(d,p)$ level of theory are displayed in square brackets.

We also examined the ISC routes from S_1 (route 2) and concluded that the routes are kinetically unfavorable. In large polyatomic molecules with a high density of the vibrational levels (the statistical limit), the ISC rate constant, k_{ISC} , is given by,⁷¹

$$k_{\text{ISC}} = \frac{2\pi}{\hbar} |\langle T_n | H_{\text{SO}} | S_1 \rangle|^2 \rho(E_{\text{ex}}), \quad (2)$$

where $|\langle T_n | H_{\text{SO}} | S_1 \rangle|$ is the norm of the spin-orbit coupling constants (SOCs) between the S_1 and triplet (T_n) states at MESXs, and $\rho(E_{\text{ex}})$ is the vibrational density of states at excess energy of E_{ex} from T_n . In Figure 12, both MESX1 (${}^1\pi\pi^*/{}^3\pi\pi^*$, S_1/T_3) and MESX2 (${}^1\pi\pi^*/{}^3n\pi^*$, S_1/T_4) are energetically lower than TS1. For the magnitude of the coupling of SOC for MESX1 and MESX2, we obtained small values. For MESX1, the value of SOC is 0.58 cm^{-1} for *m*-HMC and 0.49 cm^{-1} for *o*-HMC. These small values are reasonable from the viewpoint of El-Sayed's rule,⁷² that is that ${}^1\pi\pi^* \rightarrow {}^3\pi\pi^*$ ISC is forbidden. For MESX2, the value obtained is 11 cm^{-1} for *m*-HMC and 14 cm^{-1} for *o*-HMC, which are larger than MESX1. However, MESX2 is located at a much higher energy than MESX1 (423 and 576 cm^{-1} higher than the ${}^1\pi\pi^*$ minima of *m*-HMC and *o*-HMC, respectively). We calculated the meta-IRC in the T_4 state from MESX2 and found that the meta-IRC reaches not to the T_4 minimum but to a T_4/T_3 MECI. This means that the T_4 state does not have a stable structure along the NRD route but crosses with T_3 as the T_4/T_3 MECI at the bottom of the T_4 potential energy surface.

The MECI is located at 897 and 332 cm^{-1} below the $^1\pi\pi^*$ minima of *m*-HMC and *o*-HMC, respectively. Such a small energy gap means that the density of states ($\rho(E_{\text{ex}})$) of T_4 at MESX2 is not high enough to compete with the route of twisting along the C=C double bond. It should be noted that in both *m*-HMC and *o*-HMC, the equilibrium structure of the T_1 ($\pi\pi^*$) state is twisted at 90° with respect to the C=C double bond (see Figure S11 in the SI), similar to *p*-HMC. We thus expect a similar lifetime to that of *p*-HMC if the T_1 state is produced during the NRD process. Experimentally, we do not find a transient state with a lifetime of a few tens of nanoseconds, meaning that T_1 is not generated in the NRD process of either *m*-HMC or *o*-HMC.

We therefore conclude that most likely NRD route from the S_1 ($\pi\pi^*$) state in *m*-HMC and *o*-HMC is twisting along the propenyl C=C double bond by $\sim 90^\circ$ on the S_1 surface, which is followed by IC to S_0 via conical intersection, leading to either the *cis*-product or a return to the *trans*-form. The onset of the NRD observed in the S_1 lifetime measurement in *m*-HMC and *o*-HMC corresponds to the barrier along the isomerization coordinate in the S_1 state.

6. Conclusions

In the present study, the photochemistry involving the nonradiative decay (NRD) process and the *trans* \rightarrow *cis* isomerization after photoexcitation to the S_1 ($\pi\pi^*$) state has been

studied for *o*-, *m*- and *p*-HMC by low-temperature matrix-isolation FTIR spectroscopy, laser spectroscopic measurements in the gas phase, and quantum chemical calculations. Low-temperature matrix-isolation FTIR spectroscopy showed that all three species produce *cis*-isomerized product upon the UV irradiation. However, the isomerization requires some excess energy ($\sim 2000 \text{ cm}^{-1}$) to occur in *o*-HMC and *m*-HMC. All the molecules exhibit well-resolved S_1 - S_0 electronic spectra under jet-cooled condition. The S_1 lifetime is quite different between *p*-HMC and the other two HMCs: the S_1 lifetime is 8–9 ps for *p*-HMC³⁹ at the zero-point level, while those values are 6 ns and 10 ns for *o*-HMC and *m*-HMC at the zero-point level, respectively. The S_1 decay rate constant of *m*-HMC clearly shows an onset of the fast NRD channel at 1000 cm^{-1} above the zero-point level. In *o*-HMC, the onset of the NRD channel appears at 600 cm^{-1} . Nanosecond UV-DUV pump-probe spectroscopy indicated the production of the T_1 ($\pi\pi^*$) state in *p*-HMC, but not in either *o*-HMC or *m*-HMC. Quantum chemical calculations based on the SC-AFIR method, combined with TDDFT calculations, showed that in *p*-HMC the *trans* \rightarrow *cis* photoisomerization proceeds via a [*trans*- $S_1 \rightarrow {}^1n\pi^* \rightarrow T_1 \rightarrow$ *cis*-product] scheme. On the other hand, in *o*-HMC and *m*-HMC, this route is found to be higher in energy than another route, which is twisting along the C=C double bond by 90° on the S_1 surface, which is followed by IC to S_0 , finally leading to the *cis*-form product. The calculated barrier height along the C=C double bond twisting coordinate is in good agreement with the observed onset of the NRD channel in both *o*-HMC and *m*-HMC.

Notes

The authors declare no competing financial interest.

Acknowledgements

Y.I., M.E., and H.K. acknowledge Grants-in-Aid for Scientific Research (KAKENHI) by the Ministry of Education, Culture, Sports, Science and Technology (MEXT) Nos. 25410017, 16H04098, 16H04104, and 15KT0065, respectively. S.M., T.T., K.Y., and Y.H. acknowledge a grant from the Japan Science and Technology Agency (JST) with Core Research for Evolutional Science and Technology (CREST) in the Area of “Establishment of Molecular Technology towards the Creation of New Functions” at Hokkaido University. K. Y. is grateful for the financial supports from Building of Consortia for the Development of Human Resources in Science and Technology, MEXT. Y. H. acknowledges the financial support by JST, PREST (grant number JPMJPR16N8). T.E acknowledges the financial support from the Institute for Quantum Chemical Exploration. This work is also partially supported by the Joint Studies Program (2014-2016) of IMS. Part of the calculations in this paper was carried out by using the supercomputers at Academic Center for Computing and Media Studies, Kyoto University and Okazaki Research Facilities (Research Center for Computational Science).

ORCID

K. Yamazaki: 0000-0002-7716-6274

M. Ehara: 0000-0002-2185-0077

T. Taketsugu: 0000-0002-1337-6694

S. Maeda: 0000-0001-8822-1147

T. Ebata: 0000-0002-6236-9116

References

- (1) N. D. N. Rodrigues, M. Staniforth, V. G. Stavros, *Proc. R. Soc. London A Math. Phys. Eng. Sci.*, 2016, **472**, 2195.
- (2) L. A. Baker, B. Marchetti, T. N. V. Karsili, V. G. Stavros, M. N. R. Ashfold, M. A. Miranda, P. C. Costa, M. S. Miranda, J. C. G. E. da Silva, J. M. S. Lobo, *et al. Chem. Soc. Rev.*, 2017, **46**, 3770–3791.
- (3) L. A. Baker, S. E. Greenough, V. G. Stavros, *J. Phys. Chem. Lett.*, 2016, **7**, 4655–4665.
- (4) L. A. Baker, V. G. Stavros, *Sci. Prog.*, 2016, **99**, 282–311.
- (5) T. E. Meyer, G. Tollin, T. P. Causgrove, P. Cheng, R. E. Blankenship, *Biophys. J.*, 1991, **59**, 988–991.
- (6) M. Baca, G. E. O. Borgstahl, M. Boissinot, P. M. Burke, D. R. Williams, K. A. Slater, E. D. Getzoff, *Biochem.*, 1994, **33**, 14369–14377.
- (7) D. S. Larsen, M. Vengris, I. H. M. van Stokkum, M. A. van der Horst, R. A. Cordfunke, K. J. Hellingwerf, R. van Grondelle, *Chem. Phys. Lett.*, 2003, **369**, 563–

- 569.
- (8) K. Pande, C. D. M. Hutchison, G. Groenhof, A. Aquila, J. S. Robinson, J. Tenboer, S. Basu, S. Boutet, D. P. DePonte, M. Liang, *et al. Science*, 2016, **352**, 725–729.
- (9) C. Ko, B. Levine, A. Toniolo, L. Manohar, S. Olsen, H.-J. Werner, T. J. Martínez, *J. Am. Chem. Soc.*, 2003, **125**, 12710–12711.
- (10) Mizuno, M.; Kamikubo, H.; Kataoka, M.; Mizutani, Y. *J. Phys. Chem. B*, 2011, **115**, 9306–9310.
- (11) M. Boggio-Pasqua, M. A. Robb, G. Groenhof, *J. Am. Chem. Soc.*, 2009, **131**, 13580–13581.
- (12) G. Groenhof, L. V. Schäfer, M. Boggio-Pasqua, H. Grubmüller, M. A. Robb, *J. Am. Chem. Soc.*, 2008, **130**, 3250–3251.
- (13) L. Wei, H. Wang, X. Chen, W. Fang, H. Wang, *Phys. Chem. Chem. Phys.*, 2014, **16**, 25263–25272.
- (14) A. Xie, W. D. Hoff, A. R. Kroon, H. J. Klaas, *Biochem.*, 1996, **35**, 14671.
- (15) M. Vengris, M. A. van der Horst, G. Zgrablic, I. H. M. van Stokkum, S. Haacke, M. Chergui, K. J. Hellingwerf, R. van Grondelle, D. S. Larsen, *Biophys. J.*, 2004, **87**, 1848–1857.
- (16) I.-R. Lee, W. Lee, A. H. Zewail, *Proc. Natl. Acad. Sci. U. S. A.*, 2006, **103**, 258–262.
- (17) I. B. Nielsen, S. Boyé-Péronne, M. O. A. El Ghazaly, M. B. Kristensen, Brøndsted, S.; Nielsen, L. H. Andersen, *Biophys. J.*, 2005, **89**, 2597–2604.
- (18) D. Zuev, K. B. Bravaya, T. D. Crawford, R. Lindh, A. I. Krylov, *J. Chem. Phys.* 2011, **134**, 34310.
- (19) M. Almasian, J. Grzetic, J. van Maurik, J. D. Steill, G. Berden, S. Ingemann, W. J. Buma, J. Oomens, *J. Phys. Chem. Lett.*, 2012, **3**, 2259–2263.
- (20) E. V. Gromov, I. Burghardt, H. Köppel, L. S. Cederbaum, *J. Phys. Chem. A*, 2005, **109**, 4623–4631.

- (21) E. V. Gromov, I. Burghardt, J. T. Hynes, H. Köppel, L. S. Cederbaum, *J. Photochem. Photobiol. A Chem.*, 2007, **190**, 241–257.
- (22) E. V. Gromov, I. Burghardt, H. Köppel, L. S. Cederbaum, *J. Am. Chem. Soc.* 2007, **129**, 6798–6806.
- (23) T. Ebata, K. Saito, H. Ishikawa, N. Mikami, *Res. Chem. Intermed.*, 1998, **24**, 803–812.
- (24) N. Shida, C. Kabuto, T. Niwa, T. Ebata, Y. Yamamoto, *J. Org. Chem.* 1994, **59**, 4068–4075.
- (25) F. D. Lewis, S. L. Quillen, J. E. Elbert, S. Schneider, P. Geiselhart, *J. Photochem. Photobiol. A Chem.*, 1989, **47**, 173–179.
- (26) J. L. P. Lustres, V. M. Farztdinov, S. A. Kovalenko, *ChemPhysChem*, 2005, **6**, 1590–1599.
- (27) M. Promkatkaew, S. Suramitr, T. M. Karpkird, S. Namuangruk, M. Ehara, S. Hannongbua, *J. Chem. Phys.*, 2009, **131**, 224306.
- (28) M. Promkatkaew, S. Suramitr, T. Karpkird, S. Wanichwecharungruang, M. Ehara, S. Hannongbua, *Photochem. Photobiol. Sci.*, 2014, **13**, 583–594.
- (29) T. N. V. Karsili, B. Marchetti, M. N. R. Ashfold, W. Domcke, *J. Phys. Chem. A*, 2014, **118**, 11999–12010.
- (30) E. M. M. Tan, S. Amirjalayer, B. H. Bakker, W. J. Buma, *Faraday Discuss.*, 2013, **163**, 321–340.
- (31) S. Smolarek, A. Vdovin, E. M. Tan, M. de Groot, W. J. Buma, *Phys. Chem. Chem. Phys.*, 2011, **13**, 4393.
- (32) Y. Miyazaki, K. Yamamoto, J. Aoki, T. Ikeda, Y. Inokuchi, M. Ehara, T. Ebata, *J. Chem. Phys.*, 2014, **141**, 244313.
- (33) D. Shimada, R. Kusaka, Y. Inokuchi, M. Ehara, T. Ebata, *Phys. Chem. Chem. Phys.*, 2012, **14**, 8999–9005.
- (34) X-P. Chang, C-X. Li, B-B. Xie, C. Ganglong, *J. Phys. Chem. A*, 2015, **119**, 11488–

- 11497.
- (35) X.-Y. Xie, C.-X. Li, Q. Fang, G. Cui, *J. Phys. Chem. A*, 2016, **120**, 6014–6022.
- (36) J. C. Dean, R. Kusaka, P. S. Walsh, F. Allais, T. S. Zwier, *J. Am. Chem. Soc.*, 2014, **136**, 14780–14795.
- (37) N. D. N. Rodrigues, M. Staniforth, J. D. Young, Y. Peperstraete, N. C. Cole-Filipiak, J. R. Gord, P. S. Walsh, D. M. Hewett, T. S. Zwier, V. G. Stavros, *Faraday Discuss.*, 2016, **194**, 709–729.
- (38) Y.; Peperstraete, M. Staniforth, L. Baker, N. Das Neves Rodrigues, N. C. Cole-Filipiak, W. Quan, V. G. Stavros, *Phys. Chem. Chem. Phys.*, 2016, **18**, 28140–28149
- (39) K. Yamazaki, Y. Miyazaki, Y. Harabuchi, T. Taketsugu, S. Maeda, Y. Inokuchi, S. Kinoshita, M. Sumida, Y. Onitsuka, H. Kohguchi, M. Ehara, T. Ebata, *J. Phys. Chem. Lett.*, 2016, **7**, 4001–4007.
- (40) Y. Miyazaki, Y. Inokuchi, N. Akai, T. Ebata, *J. Phys. Chem. Lett.*, 2015, **6**, 1134–1139.
- (41) S. Maeda, K. Ohno, K. Morokuma, *Phys. Chem. Chem. Phys.* 2013, **15**, 3683–3701.
- (42) S. Maeda, Y. Harabuchi, M. Takagi, K. Saita, K. Suzuki, T. Ichino, Y. Sumiya, K. Sugiyama, Y. Ono, *J. Comput. Chem.* 2018, **39**, 233–251.
- (43) W. Hongbo, L. Yun, X. Ke, C. Bin, W. Huifei, H. Lin, Z. Hongbin, *Org. Lett.* 2015, **17**, 5974–5977.
- (44) M. J. Frisch, G. W. Trucks, H. B. Schlegel, G. E. Scuseria, M. A. Robb, J. R. Cheeseman, G. Scalmani, V. Barone, B. Mennucci, G. A. Petersson, *et al.* Gaussian 09 Revision E.01. 2009.
- (45) A. D. Becke, *J. Chem. Phys.*, 1993, **98**, 5648–5652.
- (46) C. Lee, W. Yang, R. G. Parr, *Phys. Rev. B*, 1988, **37**, 785–789.
- (47) T. Yanai, D. P. Tew, N. C. Handy, *Chem. Phys. Lett.*, 2004, **393**, 51–57.
- (48) Y. Zhao, D. G. Truhlar, *Theor. Chem. Acc.*, 2008, **120**, 215–241.

- (49) H. Nakatsuji, *Chem. Phys. Lett.*, 1978, **59**, 362–364.
- (50) H. Nakatsuji, *Chem. Phys. Lett.*, 1979, **67**, 334–342.
- (51) H. Nakatsuji, *Chem. Phys. Lett.*, 1979, **67**, 329–333.
- (52) H. Nakatsuji, *Acta Chimica Hungarica*, 1992, **129**, 719–776.
- (53) M. Ehara, J. Hasegawa, H. Nakatsuji, "SAC-CI Method Applied to Molecular Spectroscopy" in *Theory and Applications of Computational Chemistry: The First 40 Years*, pp. 1099–1141, edited by C. E. Dykstra, G. Frenking, K. S. Kim, G. E. Scuseria, (Elsevier, Oxford, 2005).
- (54) R. Fukuda, H. Nakatsuji, *J. Chem. Phys.*, 2008, **128**, 94105.
- (55) R. Fukuda, M. Ehara, *J. Comput. Chem.*, 2014, **35**, 2163–2176
- (56) R. Fukuda, M. Ehara, *Theor. Chem. Acc.* 2016, **135**, 105
- (57) M. W. Schmidt, K. K. Baldridge, J. A. Boatz, S. T. Elbert, M. S. Gordon, J. H. Jensen, S. Koseki, N. Matsunaga, K. A. Nguyen, S. Su, *et al. J. Comput. Chem.*, 1993, **14**, 1347–1363.
- (58) S. Maeda, T. Taketsugu, K. Morokuma, *J. Comput. Chem.*, 2014, **35**, 166–173.
- (59) S. Maeda, Y. Harabuchi, T. Taketsugu, K. Morokuma, *J. Phys. Chem. A*, 2014, **118**, 12050–12058.
- (60) Y. Harabuchi, T. Taketsugu, S. Maeda, *Chem. Phys. Lett.*, 2017, **674**, 141–145.
- (61) Y. Shao, M. Head-Gordon, A. I. Krylov, *J. Chem. Phys.*, 2003, **118**, 4807–4818.
- (62) J.-D. Chai, M. Head-Gordon, *Phys. Chem. Chem. Phys.*, 2008, **10**, 6615.
- (63) P. Atkins, R. Friedman, *Molecular Quantum Mechanics*, Fourth ed.; Oxford University Press: Oxford, UK, 2005.
- (64) S. Koseki, M. W. Schmidt, M. S. Gordon, *J. Phys. Chem.*, 1992, **96**, 10768–10772.
- (65) S. Koseki, M. S. Gordon, M. W. Schmidt, N. Matsunaga, *J. Phys. Chem.*, 1995, **99**, 12764–12772.
- (66) S. G. Chiodo, N. Russo, *J. Comput. Chem.*, 2009, **30**, 832–839.
- (67) S. G. Chiodo, M. Leopoldini, *Comput. Phys. Commun.*, 2014, **185**, 676–683.
- (68) X. Gao, S. Bai, D. Fazzi, T. Niehaus, M. Barbatti, W. Thiel, *J. Chem. Theory Comput.*,

2017, **13**, 515–524.

- (69) C. Adamo, V. Barone, *J. Chem. Phys.*, 1999, **110**, 6158–6170.
- (70) Some of photoexcited *m*-HMC and *o*-HMC can return to the *trans* isomers after the IC at the MECI1. The MECI1 locates on the more *trans*-side ($\phi = 98^\circ$ for *m*-HMC and 102° for *o*-HMC) than TS2 of *trans* \rightarrow *cis* isomerization in the S_0 state ($\phi = 90^\circ$). The calculated meta-IRC from the MECI1 in the S_0 state calculated reaches to the *trans*-isomer both for *m*-HMC and *o*-HMC.
- (71) C. M. Marian, *Wiley Interdiscip. Rev. Comput. Mol. Sci.*, 2012, **2**, 187–203.
- (72) M. A. El-Sayd, *J. Chem. Phys.*, 1963, **38**, 2834–2838